TECHNISCHE UNIVERSITÄT DARMSTADT

Technische Universität Darmstadt

Department of High Frequency Electronics
Prof. Dr.-Ing. Dimitris Pavlidis

Novel Diode Structures Based on Polar and Non-polar III-Nitride Semiconductors

Submitted for the degree of Master of Science in "Informations- und Kommunikationstechnik" (Information and Communication Engineering)

Author	:	B.Sc. M. Shahab Sanjari
Adviser	:	M.Sc. Eun Jung Cho
Thesis Start	:	July 1, 2008
Thesis End	:	February 02, 2009

Contents

Erklärung zur Master-Thesis gemäß §23 Abs. 7 ABP der TU-Darmstadt

Hiermit versichere ich, die vorliegende Master-Thesis ohne Hilfe Dritter nur mit den angegebenen Quellen und Hilfsmitteln angefertigt zu haben. Alle Stellen, die aus den Quellen entnommen wurden, sind als solche kenntlich gemacht worden. Diese Arbeit hat in gleicher oder ähnlicher Form noch keiner Prüfungsbehörde vorgelegen.

Darmstadt, im Februar 2009

_____

B.Sc. M. Shahab Sanjari

بسم الله الرحمن الرحيم

In the Name of God, The Compassionate, The Merciful

Zusammenfassung

Neuartige Diodenstrukturen basierend auf polaren und nicht polaren III-Nitridhalbleitern

Diese Arbeit befasst sich mit den Möglichkeiten der Realisierung von Resonanz-Tunneldioden auf Basis von polarem und nicht polarem Galliumnitrid.

Zunächst werden die Materialeigenschaften vom Galliumnitrid und Aluminiumnitrid behandelt. Anschließend werden einige Themen aus der Theorie der Berechnung von Heterostrukturen beschrieben. Die Ergebnisse der Simulation werden ebenso vorgestellt.

Strukturen mit einer und zwei Quantumbarrieren wurden gewachsen und mittels Standard-Kontaktlithographie verarbeitet. Die hergestellten Dioden wurden elektrisch gemessen und charakterisiert. Die erzielten Ergebnisse wurden anschließend mit der vorhandenen Literatur verglichen.

Acknowledgments

All of this work would have not been possible without the encouraging support of Professor Dr.-Ing. Dimitris Pavlidis to whom I am much thankful.

I wish to express my sincerest gratitude to my adviser, Mrs. M.Sc. Eun Jung Cho, who supported me patiently through the work.

Many thanks goes to Mr. Dr.-Ing. Sanghyun Seo for providing me with helpful suggestions. I would like to thank Mr. M.Sc. Chong Jin for his help in the lab, and Mr. Dr.-Ing. Oktay Yilmazoglu for his practical hints during the work.

I would like to dedicate this work to my dear mother and father, to whom my absence during the studies had been most unpleasant, and to my wife, Marina for her patience.

1 Introduction

In 1958 Esaki[1] first introduced Tunneling effect in semiconductor diodes [1]. Tunnel diodes promised many new characteristics and circuits which were very interesting for signal generation and amplification, remote sensing, medical applications and other areas where high frequency signals were required.

Tunnel diodes were originally made using silicon. They showed a negative differential resistance in their I-V characteristic curve which could be used to make oscillators. These diodes have heavily doped p-n junction and used the effect of the transition of the electron from the conduction band of the n-side to the valence band of the p-side. But soon researchers realized that these diodes were not suitable for applications since their characteristics could not be altered so easily [2]. This caused a long sleep of the technology of the tunnel diodes after that.

Soon after, as alternative semiconductors started to gain more popularity, researchers started to think about incorporating these new compound semiconductors in the device structures. So like many other new devices such as high electron mobility transistors, etc., resonant Tunneling diodes (RTD) were made out of compound semiconductors.

Gallium arsenide (GaAs) was the pioneering material of the III-V compound semiconductors. Using GaAs many researchers introduced among other devices resonant tunneling diodes which were successfully used in high frequency circuits for signal generation. Most of the gallium arsenide based RTDs used layers of sequentially changing of a lower bandgap material (GaAs) and a wider bandgap material (AlGaAs) as a potential barrier. Detailed explanation of the these devices and how they work will be presented in chapter 3.

RTDs were fabricated in planar and non planar types. The planar structure is mostly preferable since it is possible to incorporate the device on the same substrate where passive devices also reside, in order to form the so called microwave monolithic integrated circuits (MMIC). In non-planar type of RTDs the contacts are placed on top and bottom of the device. This poses some fabrication difficulties but in most cases a better quality of charge transport is achieved since the charges won't propagate laterally. Most of the RTDs are also connected to some sort of wave guiding setup which enables the insertion and extraction of the signal and let it propagate forward. One of the many successful RTDs fabricated with GaAs is fabricated by Orihashi et. al. [3], where oscillation in 1THz region have been achieved.

---

[1]Leona (Leo) Esaki (1925 − present), Japanese physicist.

RTDs can be an alternative to the existing solid state signal generation devices such as Impact Avalanche Transit Time (IMPATT) and Gunn[2] diodes. RTDs could be fabricated in much smaller dimensions and could be integrated with other circuit elements. The advantages over the non solid state signal generation methods are obvious, except where extremely high power signals are needed in the 200 GHz range, where the tube based generators (such as Gyrotrons and Klystrons) are still in use.

As the silicon technology caught up with the speeds that GaAs was originally promising, other group III and V compounds like *Indium phosphide* (InP), *Gallium nitride* (GaN) and even some group II-V compounds like *Zinc oxide* (ZnO) were introduced. The state of the art GaAs technology is well established. Other compound semiconductors promise new application areas because of their unique characteristics but their technology is not so well established, and their theory is not as well studied as GaAs.

Among many existing compound semiconductors, Gallium nitride was one of the successful materials of the recent years, due to its exceptional thermal and mechanical stability and its wide bandgap. Like GaAs, GaN could be grown epitaxially and be processed with standard wafer level operations. This promised a good start in the GaN technology. Soon achievements made in GaN technology and device fabrication took some prominent position in the scientific literature of applied solid state physics and technology.

In the 1990s, one of the major achievements in the GaN technology was the blue light emitting diode (LED) and later the blue laser diode (LD) which were both a great commercial success. But, still getting larger wafers, freestanding GaN substrates and reliable fabrication are a concern of the researchers and subject of many scientific publications and dissertations.

More intensive study of the charge transport inside of the GaN devices showed that due to the crystall structure, large electric fields exist at the heterostructure interface of the GaN and AlN or GaN and AlGaN. These effects are desireable in the horizontal structures where the presence of these fields form a charge accumulation which actually enhances charge transport. This so called two dimensional electron gas (2DEG) shows a great advantage over the traditional GaAs based HEMT structures in these structures. The intensive study of the Metal Insulator Field Effect Transistor (MISFET) structures and other two dimensional devices such as Metal Semiconductor Field Effect Transistors (MESFET) and High Electron Mobility Transistors (HEMT) shed light on the lateral charge transport inside layered structures of GaN. The vertical charge transport on the contrary, has been less frequently subject of research.

Even worse, the polarization field is reported as a problem in the vertical transport of the charges inside a diode. Here the band bending and the charge accumulation are not desirable. Some negative effects on the existing light emitting diode technology where the red shift of the radiation which causes inaccuracy of the emitted spectrum

---

[2]John Battiscombe Gunn (1928 − present), Egyptian-born US/British physicist.

[4], [5].

Since the structure related induced electric fields were inherent in the nature of these problems, researchers tried to examine the the crystal structure of GaN and find a possibility to grow the semiconductor in a direction where the crystal shows symmetry. This way one might be able to overcome the asymmetry in the direction of charge transport which cases band bending and change in the carrier energies. Also the piezoelectric polarization fields are not dominant in the non polar growth directions.

Flat GaN bands as in Gallium arsenide would be a revolutionary success in making precision devices and circuits. One of the mostly used non-polar growth directions is the (1 1 $\bar{2}$ 0) direction. GaN grown in this direction is called "a-plane GaN". The term is used on the contrary to the traditional growth direction along the z axis of the hexagonal structure, the (0 0 0 1) direction, or the "c-plane GaN", where the numbers in the parentheses are the so called Miller[3] indices. Throughout this text the terms *a-plane* and *c-plane* are used frequently.

This work concentrates on studying the polarization in single barrier and double barrier quantum structures using polar and non-polar nitrides in order to achieve realization of a resonant Tunneling diode.

1.1 Motivation

Resonant tunneling diodes made of c-plane GaN are still rarities. Except in optoelectronics, other devices made with a-plane GaN are also not so frequently subject of research. To the authors knowledge, no RTDs have been made using a-plane GaN.

The motivation of this work is to investigate single and double barrier quantum structures and their characteristics. These structure were designed and simulated in order to understand the charge transport across vertical structures.

This work has unique points since no previous work on RTDs are known to the author which are grown entirely with MOCVD. Also investigations of growth of single barrier structures on top of r-plane sapphire are rare.

---

[3]William Hallowes Miller (1801 − 1880), British mineralogist and crystallographer

2 Properties of III-Nitrides

Nitride semiconductors have gained increasing popularity in research and industries. They have outstanding optoelectronic characteristics. They have a direct bandgap and their bandgap can be engineered by forming ternary and quaternary alloys. This has allowed application of nitride semiconductors in high frequency high temperature systems. Furthermore the III-Nitrides are inert, which makes them suitable for sensors in gaseous and liquid environments [6].

The pyroelectric[1] characteristics of the nitride semiconductors can also be used to form new electronic devices such as sensors for detection of ions, gases and polar liquids [7].

In this chapter growth technologies and important material properties of III-nitrides will be presented.

2.1 Growth Technologies

III-Nitrides share some of the common growth techniques which are used for the growth of conventional III-V semiconductors. Each technique has their particular applications and usages, their advantages and disadvantages.

2.1.1 Metal Organic Vapor Phase Epitaxy

Metal organic vapor phase epitaxy (MOVPE) produces high quality GaN with reasonable growth rate and using moderate amount of resources. For this reason MOVPE has become more or less the industry standard for production of GaN devices such as blue light emitting diodes and laser diodes.

MOVPE or in our case MOCVD (Metal Organic Chemical Vapor Deposition) utilizes either a horizontal or a vertical reactor chamber. The Thomas Swan[2] MOCVD system used in this work is of the vertical type, with a susceptor capable of holding up to three wafers. This equipment is depicted in Figure 2.1. The metalorganic compounds are stored in vessels which are stored in temperature controlled baths. The carrier gas (Nitrogen or Hydrogen) is passed through these vessels and carries metalorganic molecules with it into the reactor chamber. Ammonia (NH_3) gas bottle

---

[1]Pyroelectricity is the ability of certain materials to generate an electrical potential when they are heated or cooled.
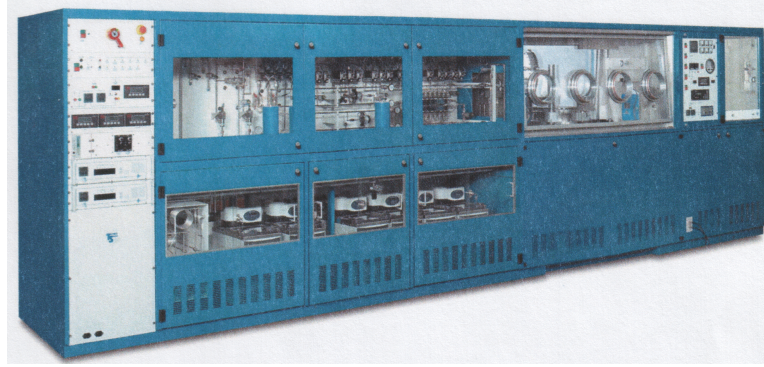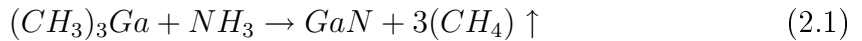
[2]www.aixtron.de

Figure 2.1: Our MOCVD equipment in the lab [8]

is also connected to the machine and acts as the nitride source. Using computer controlled valves, these compounds are guided through pipes into the main reactor chamber and optionally together with doping material. The main reaction for growing GaN is[3]:

$$(CH_3)_3Ga + NH_3 \rightarrow GaN + 3(CH_4) \uparrow \tag{2.1}$$

This reaction takes place on top of the hot substrate where the gas molecules are broken and the desired material is deposited. For p-doping of GaN, Cp_2Mg (Bis Cyclopentadienyl Magnesium) is used which is also stored in one of the bubbler vessels. For n-doping, Silane (SiH_4) is used which comes directly from the gas bottle.

The susceptor is heated using a tungsten heater. This heater is divided into three different zones A, B and C. These heating zones should be switched and set during the growth in an appropriate sequence. Due to the distance between the point where a thermocouple is located below the substrates under the surface of the susceptor, measurement of the exact temperature of substrates is not possible. So a calibration is needed and it is done from time to time with a calibration set. During the growth, the susceptor rotates which facilitates uniform deposition of material on top of the substrates.

2.1.2 Molecular Beam Epitaxy

Molecular beam epitaxy (MBE) can produce high quality GaN with abrupt interfaces. High quality growth achieved by MBE could be controlled at atomically sharp interfaces. For the growth of GaN, conventional MBE is not suitable, therefore a variant of MBE, either plasma assisted (PAMBE) or laser assisted is used because N_2 cannot dissociated by using conventional effusion cells. Plasma source (RF or electron cyclotron resonance plasma) can be used to activate N_2 [9].
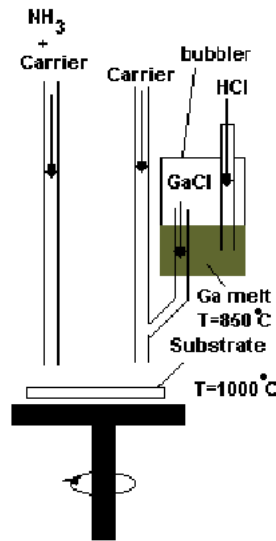
---

[3]$\uparrow$ denotes gas form.

Figure 2.2: Schematic of vertical HVPE reactor [9]

The high quality of the MBE has its costs: for MBE ultra high vacuum is needed and growth rate is very slow. Large amounts of Nitrogen is needed during the process and the whole setup and its maintenance is very expensive.

2.1.3 Hybrid Vapor Phase Epitaxy

Hybrid vapor phase epitaxy can produce GaN bulk material with a large growth rate (up to $100 \mu m/h$). The quality is not comparable with the other two techniques described above, but the high growth rate makes this method attractive for growing free standing GaN substrates [10]. HVPE cells could be made horizontally or vertically. The vertical reactor facilitates the rotation of the samples. Inside the reactor, Nitrogen is used as carrier gas.

The temperature of the growth zone is kept about $860°C$. In the growth zone $GaCl$ and NH_3 come to reaction as follows:

$$GaCl + NH_3 \rightarrow GaN + HCl + H_2 \tag{2.2}$$
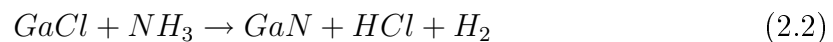
Figure 2.2 shows a vertical HVPE reactor. One of the main drawbacks of the HVPE technique is that the side reaction of the Nitrogen with HCl which produces NCl_3 that itself is highly explosive. Another drawback is the undesired reaction and deposition of the wall of reactor. Also care should be taken that HCl doesn't come in contact with air, which will quickly destroy the reactor. By-products like $GaCl_3$ and NH_3Cl could also condense and clog the exhaust lines unless heated above $150°C$. P doping is more difficult with HVPE process [9] compared to MOCVD and MBE

processes.

2.2 III-Nitrides Characteristics

Of the existing III-Nitride semiconductors, Boron nitride, Aluminum nitride, Gallium nitride and Indium nitride and specifically the last three ones, are mostly used. These could be found in three different crystal forms, namely the *rocksalt*, the *zinc blende* (also known as *sphalerite* or *β-polytype*) and the *wurtzite*, the last being the most stable in the room temperature [11]. Except for the BN which is available in zincblende structure, other compounds could be epitaxially grown to get such a formation under high pressure conditions. The cubic rocksalt formation could be achieved only in very high temperatures for III-nitrides. Since nitrides investigated in this work have wurtzite form, this structure will be described in the following section.

2.2.1 Wurtzite Crystal Structures

The wurtzite structure is hexagonal as depicted in Figure 2.3 with its two lattice constants **a** (in plane lattice constant) and **c** (out of plane lattice constant). It is usual in the crystallography to study the structure of the crystals using Miller indices which are traditionally **l**, **m** and **n**. This numbering system is quite satisfactory in the cubic structures, but for the wurtzite structure, a four-number system is used which is called Bravais[4]-Miller index **h, k, i** and **l**. In this system

$$i = -k - h \qquad (2.3)$$

is a redundant number which is written between k and l as (*hkil*). h, k and l are the same as traditional Miller indices **l**, **m** and **n**. The redundant number helps identifying different permutations. By convention, negative integers are written with a bar on top.

In wurtzite crystal structure polar planes exist. These polar planes are cuts through the crystal where on each side of the cut, either group III atoms or group V atoms exists. The primary polar plane for the wurtzite structure is called the **basal** direction or (0 0 0 1) plane. On every cut the atoms along the c-axis, the surface terminates either with group three or with group five atoms.

Depending on which atomic layer is the last on the surface, for example in the case of GaN, the material is called **Ga-faced** or **N-faced**. The growth technique decides on the face of the materials. The surface of GaN grown with MOCVD is terminated with Ga face while in case of MBE both faces are possible. Since the throughout this study, MOCVD process has been used, the material used in this work are Ga-faced.

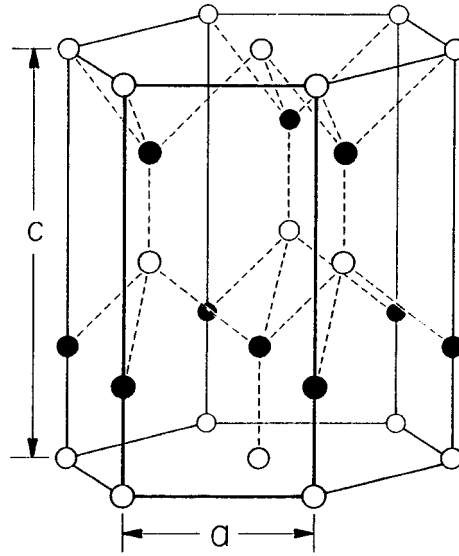[4]August Bravais $(1811 - 1863)$, French physicist.

Figure 2.3: The wurtzite crystal structure [11]

Unlike in zinc blende crystal structure, where all bonds have equal length, in wurtzite structures, there are two slightly different bond lengths. The growth in the basal direction (along the z axis) shows a large asymmetry in the structure. This asymmetry causes the an internal electric field in this direction which causes accumulation of charge carriers on the GaN side of the interface. This is the origin of the **spontaneous polarization** charges in the bulk of GaN and AlN. Same is with the ternary compound of AlN and GaN (AlGaN).

Growing Aluminum nitride on top of GaN follows the same hexagonal trend. In Figure 2.3 in case of a GaN crystal, the white circles show the Gallium atoms (or Aluminum in the case of AlN) and the black circles are Nitrogen atoms. So on the top most layer we have a layer of Gallium atoms. If we stop the growth of the GaN and start growing AlN, we will have Aluminum atoms on top of the structure of the Figure 2.3 with another Nitrogen layer to follow and so on.

Since the lattice constant of AlN is smaller than that of GaN, besides the spontaneous polarization, the strain induced polarization field (**piezoelectric polarization**) is also present which is a result of the lattice mismatch between two layers of the heterostructure quantum well e.g. AlN and GaN. Spontaneous and piezoelectric charges add up and make a strong built in electric field. The direction of these fields are depicted in Figure 2.4.

The key point in avoiding these charges is to grow the crystal in a direction along which the crystal shows symmetry (see Figure 2.5 bottom) and therefore spontaneous and piezoelectric polarizations are not dominant any more. In practice, this is achieved using a sapphire wafer which is cut in the **r-plane** direction. GaN grown on
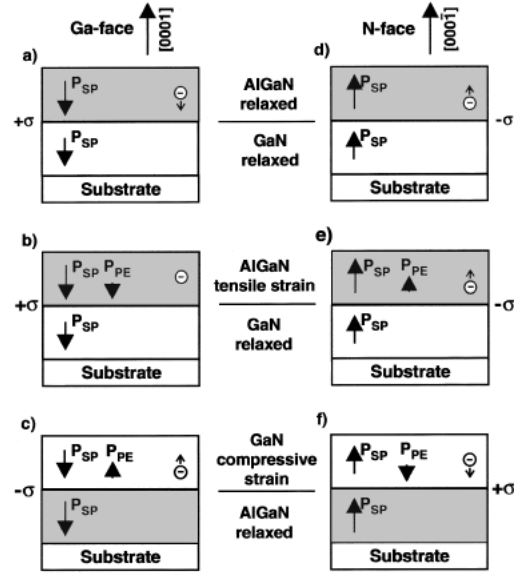
Figure 2.4: Directions of spontaneous and piezoelectric polarization [12]

top of such sapphire substrate is called a-plane GaN. This is schematically depicted in Figure 2.6.

2.2.2 Polar vs. non-polar GaN

In the example of c-plane InGaN/GaN quantum wells, induced polarization fields of about $1MV/cm$ could be present [14]. These could result in band bending in hetero interface regions. Also in light emitting diode structures, the resulting 2DEG due to the built-in electric field decreases the overlapping of electron and hole wave functions which in turn causes separation of electron and hole pairs (**exitons**) in the quantum well, although still bound inside the well. This is called the **quantum confined Stark**[5] **effect** and it significantly reduces carrier recombination rate in quantum wells. The emission of the LEDs will therefore have a red shift due to slow recombination of charge carriers.

For electron devices such as a HEMT it is desirable to have normally off operation. This provides safe operation even with a sudden release of the Gate bias and makes GaN devices comparable with current Silicon technology [13]. The induced 2DEG causes high sheet carrier concentrations of order of $10^{13}cm^{-2}$ which make a possible normally-off operation difficult. Apart from reduction of carrier concentration by epitaxial design [15] and recessed gate structure [16], non-polar a-plane GaN could be used to overcome such problems.

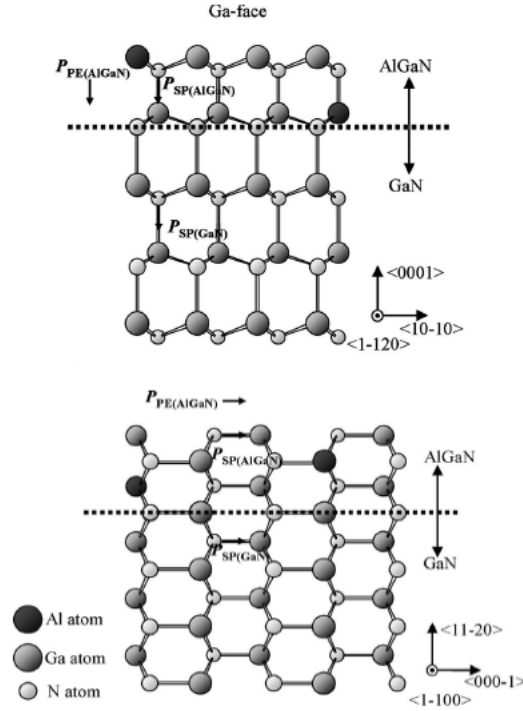[5]Johannes Stark $(1874 - 1957)$, German physicist.

Figure 2.5: Arrangement of the atoms at the interface of AlN and GaN [13]

In this work non polar GaN is aimed to use for the resonant tunneling diodes. Flat energy bands as a result of no polarization field in GaN will allow determination carrier concentration only due to doping and the diode structure will have symmetric I-V characteristics.

2.2.3 Properties of GaN and AlN

GaN is a very robust semiconductor material with high thermal stability. It could be doped with Silicon to form n-doped GaN. AlN is one of the non-metallic diamond like compounds (together with SiC, BeO and cubic BN). These compounds have high temperature stability and thermal conductivity and are very hard. AlN could almost be considered as an insulator with its large bandgap, but its semiconducting characteristics makes this material an interesting choice for quantum barriers for GaN based devices. Table 2.1 shows material parameters of GaN and AlN which are considered mainly in this work. For comparison, other semiconductors are also included.

Properties of AlGaN is usually calculated in relation to AlN and GaN using Vegards's law which indicates that at a constant temperature, the lattice constant of
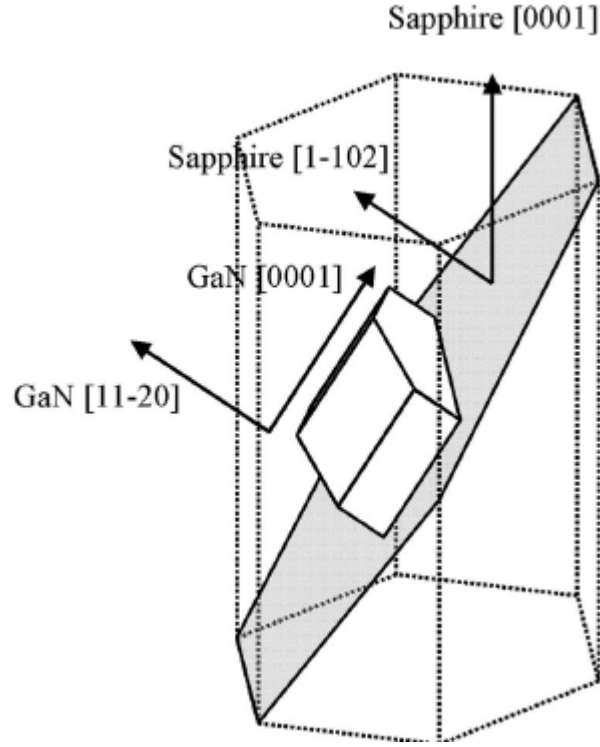
Figure 2.6: Schematic representation of crystal directions in sapphire and GaN [13]

Material	c [Å]	a [Å]	ϵ_r	E_g [eV]	$\mu_e[cm^2V^{-1}s^{-1}]$	$\mu_h[cm^2V^{-1}s^{-1}]$
AlN	4.9	3.11	8.5	6.22	683	14
GaN	5.18	3.18	9.7	3.434	1478	30
GaAs	–	5.65	13.1	1.424	8500	470
Si	–	5.43	11.9	1.124	1430	460

Table 2.1: Comparison of some material properties [17].

an alloy has linear relation with the lattice constants of the constituent crystals. In-creasing the mole fraction of AlN increases the bandgap and the effective mass until respective values of AlN are reached.

3 Theoretical Background

In this chapter, theoretical background of resonant tunneling will be covered. Some concepts needed for RTD simulations will be discussed. These simulations are based on theoretical models incorporating quantum mechanical studies of the semiconductor physics. The basic concepts and theory of simulation used in this work will be described.

In the simplest form an infinite single quantum well could be assumed. The calculation basis then extends to multiple quantum wells and finite versions of both. Same calculation is carried out for a single quantum barrier which extends to multiple quantum barriers. Each of the quantum wells or barriers could in general be asymmetric. Also one could differentiate between type-I and type-II multiple quantum wells. In the type-I systems electrons and holes reside in the same quantum region whereas in type-II systems, they are separated (see Figure 3.1). Type-I systems allow fast recombination of the excited electron states which is more desired in laser diodes. Band engineering allows such variations in the structure.
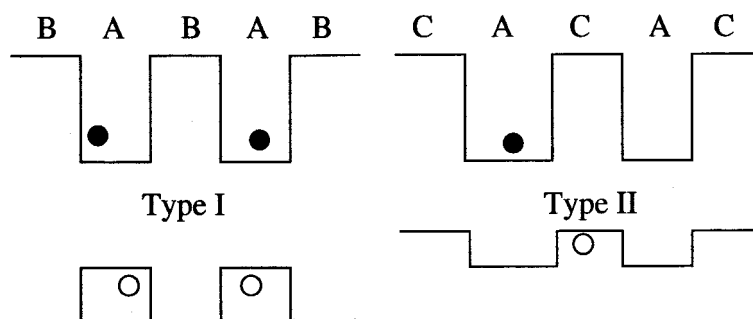

Figure 3.1: The one dimensional superlattice in Type-I and Type-II double barrier systems [18].

3.1 Numerical approaches and Simulation

Computer based simulation techniques are used to model semiconductor parameters and their behavior in a device. Due to cost effusiveness, device level simulation is an important part of semiconductor engineering. Most of the device simulators are

capable of performing 1D, 2D or sometimes 3D simulations of the energy levels, band structures, local density of states and even current and charge distributions across layered structures of the devices. A detailed description of the existing simulators could be found in [17].

λ, the de Broglie[1] wavelength of a particle and p, its momentum, are related to each other through the Plank's[2] constant, h:

$$\lambda = \frac{h}{p} \tag{3.1}$$

.

An electron in vacuum in position $\mathbf{r}$ far from any disturbances and electric potentials could be described with *state function*

$$\psi = e^{j(\mathbf{k} \bullet \mathbf{r} - \omega t)} \tag{3.2}$$

which is in form of a wave, with $j = \sqrt{-1}$, ω being the angular frequency, t the elapsed time and $\mathbf{k}$ the wave vector whose magnitude $|\mathbf{k}| = 2\pi/\lambda$. The **wave function** is a function of position of the particle, $\psi(x, y, z)$ and describes the probability of finding the particle in (x, y, z) at time t [19]. The wave-like behavior of the particles are more pronounced where the matter wavelengths are comparable to interatomic spaces.

The quantum mechanical momentum acts as an eigenvalue on the wave function ψ as:

$$-j\hbar \nabla \psi = \mathbf{p} \psi \tag{3.3}$$

with $\mathbf{p}$ being $\mathbf{p} = \hbar \mathbf{k}$ and $\hbar = h/2\pi$ which is often called Dirac's[3] constant. The total energy of a particle in this wave description is called the time independent Schrödinger[4] equation:

$$-\frac{\hbar^2}{2m_e} \nabla^2 \psi = E\psi \tag{3.4}$$

with m_e being the mass of the electron and E its energy. This is valid for an electron in vacuum, but in confined spaces wave functions must satisfy certain boundary conditions, which in turn introduces discrete energy modes as shown in Figure 3.2. In crystals many atoms are placed near each other, therefore the crystal potentials becomes complex. For simplicity it is assumed that the mass of electron is constant throughout the crystal and an empirical fitting parameter called *effective mass* (m^*) is introduced.

---

[1]Louis-Victor de Broglie (1892 − 1987), French physicist
[2]Max Karl Ernst Ludwig Planck (1858 − 1947), German physicist
[3]Paul Adrien Maurice Dirac (1902 − 1984), British physicist
[4]Erwin Schrödinger (1887 − 1961), Austrian physicist

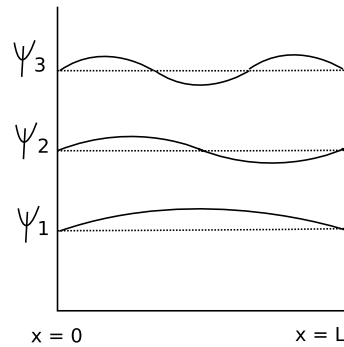Figure 3.2: The first three allowed standing waves for a particle in a box [19].

$$-\frac{\hbar^2}{2m^*}\nabla^2\psi = E\psi \tag{3.5}$$

with the energy solution being

$$E = \frac{\hbar^2 k^2}{2m^*} \tag{3.6}$$

This is called the **effective mass approximation**. The effective mass approximation is best in low electric fields where electrons have low momenta [18]. More information on effective mass approximation could be found in [20].

It is worth noting that in these calculations, an assumption has been made that the crystal is infinitely periodic so that the propagation of eigenenergies can be thought to be like plane waves in vacuum.

The above theory could be extended to calculate bulk semiconductors and hetero structures. The **envelope function approximation** makes also use of effective mass approximation. It states that if effective mass approximation could be assumed for each single layer of a heterojunction, then the effective mass approximation could also be assumed to be valid for the heterojunction itself, and even multiples of these heterojunctions. Using envelope function approximation, one could solve the 1-D Schrödinger equation for the whole system [18].

In a more realistic model, at a heterojunction, apart from different effective masses, other properties such as different band offset, different dielectric and lattice constants could be taken into account.

3.2 Solution Techniques

One of the mostly used methods for the numerical calculation of the Schrödinger equation is the **shooting method**. For simplicity, the one dimensional Schrödinger equation is considered again as below:

$$-\frac{\hbar^2}{2m^*}\frac{\partial^2}{\partial z^2}\psi(z) + V(z)\psi(z) = E\psi(z) \tag{3.7}$$

where effective mass and envelope function approximations are assumed. Expanding the first and second order derivative of the wave function, the above equation could be brought in the form of [18]

$$\psi(z + \delta z) = \left[\frac{2m^*}{\hbar^2}(\delta z)^2(V(z) - E) + 2\right]\psi(z) - \psi(z - \delta z) \tag{3.8}$$

Then using two known values of the wave function $\psi(z - \delta z)$ and $\psi(z)$, a third value such as $\psi(z + \delta z)$ could be predicted. The initial and boundary conditions used could be generalized to make this method also suitable for non symmetric structures.

An account for variable effective mass could be made by replacing m^* with $m^*(z)$ where the z dependency is obvious. This could be used to care for the one dimensional calculation through heterostructure with several different layers.

$$\frac{\partial}{\partial z}\frac{1}{m^*(z)}\frac{\partial}{\partial z}\psi(z) = \frac{2}{\hbar^2}[V(z) - E]\psi(z) \tag{3.9}$$

In the above equations, in the simplest assumption, $V(z)$ could be the edge of the conduction band of a double barrier structure. This equation cannot be expanded by finite difference methods since $\partial m^*(z)/\partial z$ has discontinuities and the results will be inaccurate. More details on suitable expansion methods can be found in reference [18].

Applying an **electric field** at both sides of the heterostructure tilts the energy band as depicted in Figure 3.3 for a double quantum well structure, where the solid line describes the zero bias and the dashed line shows application of bias as indicated in the figure.

Instead of $V(z)$ in the previous section, $V'(z)$ is used as below:

$$V'(z) \longrightarrow V(z) + qF(z - z_0) \tag{3.10}$$

where F is the electric field[5], z_0 being the origin of the field often used in the center of the structure and $q = -e$ for an electron an $q = +e$ for a hole [18]. This equation indicates that on each iteration the voltage caused by the additional electric field will be added to the previous voltage seen by the charge carrier. Due to the application of electric field, a depletion region appears at the left side. In the case of III-Nitride heterostructures as described in the previous chapter, the external electric field might need to fight back or enhance the built-in electric field inside the heterostructure.

So far the calculations have focused on a single charge carrier. But in reality, the conduction band contains more than one charge carrier. Such carriers might give

---

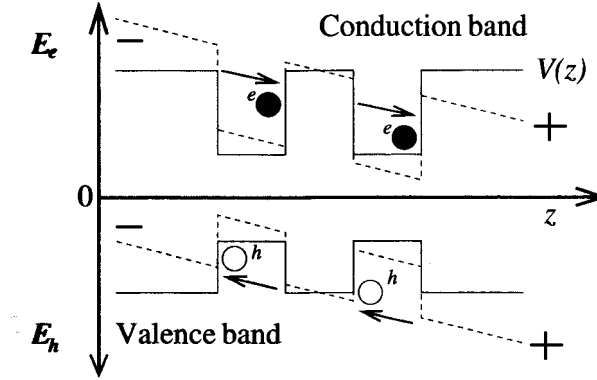[5]Usually E is chosen for electric field but here we use F and save E for energy.

Figure 3.3: Band tilting due to the application of an electric field[18]. Solid lines describe zero bias and dotted lines describe positive bias

rise to additional voltages on top of the usual band edges when they come together. These additional charges are so high in GaN that could pose an order of magnitude difference. For this reason the electrostatic field describing the system needs to be calculated using the **Poisson's**[6] equation.

Imagining a system where equal number of ionized impurities and electrons exist i.e. charge neutrality could be assumed, and imagining any kind of charge distribution e.g. caused by a δ-doping or the previous calculation of the charge caused by application of an electric field, the additional potential V_p could be calculated by

$$\boxed{\nabla^2 V_\rho = -\frac{\rho}{\epsilon}} \tag{3.11}$$

which is the Poisson's relation, with ρ the charge density and $\epsilon = \epsilon_r \epsilon_0$ is the permittivity of the material[7]. The general solution is then obtained by the traditional method:

$$V_\rho(\mathbf{r}) = -\int_{-\infty}^{\mathbf{r}} \mathbf{F} \bullet d\mathbf{r} \tag{3.12}$$

where $\mathbf{F}$ is the electric field and $\mathbf{r}$ the position vector. By replacing $V(z)$ in equation 3.7 with

$$V(z) \longrightarrow V_{CB}(z) + V_\rho(z) \tag{3.13}$$

where V_{CB} is the band edge potential at zero doping and V_ρ the potential due to the non zero number of the carriers [18]. This equation is solved iteratively, each time calculating the amount of charge for a step and then adding it for the next calculation

---

[6]Siméon-Denis Poisson 1781 − 1840), French mathematician, geometer, and physicist.

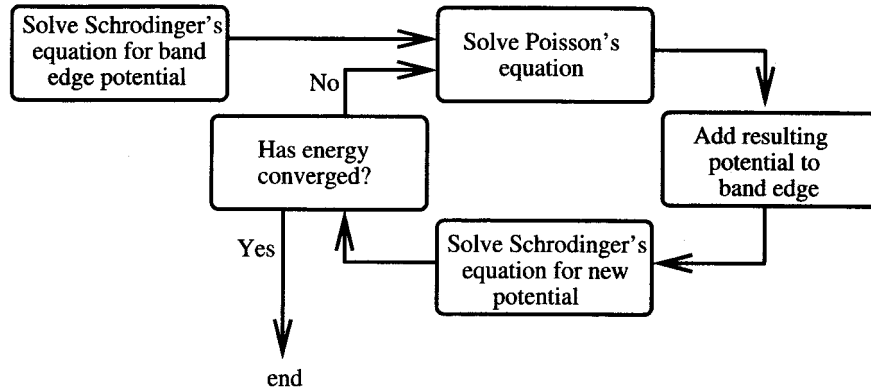[7]ϵ_r is the relative permittivity constant and ϵ_0 is the permittivity constant of vacuum.

Figure 3.4: Block diagram of self consistent iteration [18].

step to $V(z)$. For each loop, the Schrödinger equation is solved once. This process is called **self-consistent** calculation of the Schrödinger-Poisson equation which is repeated until convergence of the energy eigenvalues is reached. There are other alternatives to this method such as Hartree's[8] many electron approach which is not covered in this text.

3.3 Bandstructure calculations

In the simulation of RTDs, three of the mostly used assumptions are:

- Effective mass band structure [21].

- Thomas[9]-Fermi[10] charge screening where the effect of quantization in emitter region and charge in well region is not considered [22] .

- Esaki-Tsu[11] current density formula where in the 1-D integral the transverse momentum and energy are assumed to be separable [23].

Each of these assumptions reduce the complexity of calculations to some extent, but also restrict accurate prediction of experimental results. In this chapter the first assumption which is mainly related to this work is described.

More information on the second topic which is how Hartree model could be used to improve electrostatic potential and the charge screening could be found in [24]. Also in the same work, it is shown that numerical integration over the transverse momentum offers improved subband alignment over the Esaki-Tsu model.

---

[8]Douglas Rayner Hartree $(1897 - 1958)$, English mathematician and physicist

[9]Llewellyn Hilleth Thomas $(1903 - 1992)$, British physicist and applied mathematician.

[10]Enrico Fermi $(1901 - 1954)$, Italian physicist.

[11]Raphael Tsu, Chinese physicist.

The movement of carriers in a semiconductor is bound by the crystal forces. Using the Schrödinger equation and Hamiltonian[12] matrices we can determine the eigenenergies and eigenstates as described in the previous section. After computing the Schrödinger equation we get a complicated energy-momentum E(k) relationship.

$$E(k) = f(k) \tag{3.14}$$

The valence band may look like a parabolic curve, but the conduction band mostly doesn't since the there are crystal forces which apply to the electron, so the curves have dispersion.

The **dispersion diagram** has two parts of attenuation and propagation. Now remembering the expression for the wave function in the right hand side of the $E(k)$ diagram

$$\psi \propto e^{jkr} \tag{3.15}$$

there is also a complex band which connects the valence and conduction band. This happens on the negative side of the $E(k)$ diagram where the states are attenuated instead of being propagated, i.e. an incident energy into the bandgap of the material will be attenuated. If a plane wave is injected into the barrier it would be attenuated. Assuming the same parabolic decay with the same effective mass we can calculate the attenuation constant κ. But again, since the valence and conduction bands are connected to each other via a complex band, the attenuation constant κ is in reality smaller than when we would be reading from the parabolic attenuation.

$$\psi \propto e^{-jkr} \tag{3.16}$$

Figure 3.5 shows the band structure of a typical III-V. The dashed lines is obtained with the **ten band nearest neighbor ($sp3s^*$) model** (also called the **full band model** or simply **ten band model**) while the dotted lines indicate calculations with the **single band effective mass model**. In the so called *single-band* model, the dispersion of the bands in the $E(k)$ diagram is ignored and a parabolic shape for the bands are assumed. Also it is assumed that bands are **decoupled** which means the **complex band wrapping** in the bandgap region is ignored. The single band model does not incorporate the real and imaginary band non-parabolicity. This causes calculations for RTDs to be inaccurate since the simulation results by employing the single band model were found to be different from the experimental results in reference [24] as below:

- It predicts a peak resonance current that is a factor of three less than experiment,

- The second turn on voltage is predicted to be at much higher voltages.

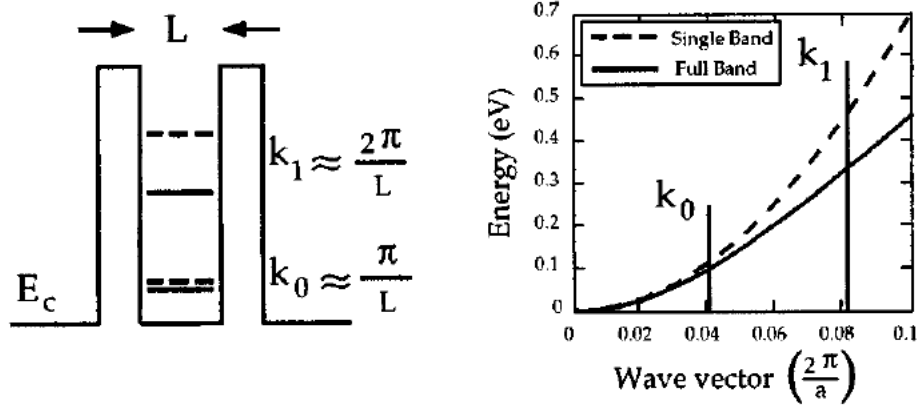[12]Sir William Rowan Hamilton $(1805 - 1865)$, Irish mathematician

Figure 3.5: (Left) Approximate resonant energies. (Right) Band structure of a typical III-V calculated by full (ten) and single band models [24].

Assuming parabolic bands in a double barrier resonator, where L is the resonator length, the ground level resonance is $K_0 = \frac{\pi}{L}$ the first excited level is on $\frac{2\pi}{L}$, that is resonances occur at $\frac{2\pi}{L}$, $\frac{4\pi}{L}$, etc. of the well length with L being the well width. The resonance locations are given by the energies corresponding to these wavelengths on the $E(k)$ diagram. As it could be seen in Figure 3.5, the right side diagram shows that since the single band model is parabolic, the dispersion shown is increased compared to the non-parabolic case. This in turn shows a higher exited energy as shown in Figure 3.6 and accounts for higher turn on voltage [24] which causes higher turn on voltages. Also the **valley current** is underpredicted at least by two orders of magnitude [24]. Barriers are much more transparent than the single band model would suggest. So for the same eigenenergy of the system, the current peak is higher than in the single band model. The complex band wrapping suggests a lighter effective mass which could be seen in Figure 3.7 (left), i.e. a particle which is tunneling through the bandgap will be less attenuated in reality than is suggested by the single band model.

In real semiconductors, complex bands connect two real bands as depicted in Figure 3.7 (right) and are not parabolic. In the single band model in contrast an assumption is made that these bands are parabolic. Now assuming we have a barrier which is so high as the half of the mid bandgap. Then for a tunneling through this barrier the k predicted by the single band model is higher than the one predicted by the full band model. This in turn means that the single band model predicts the bandgap having much more attenuation than the ten band model. This is schematically depicted in the bottom left part of Figure 3.7. Resonance widths predicted by the single band model will be smaller than reality and result in lower tunneling currents [24]. This aspect is shown in Figure 3.8.
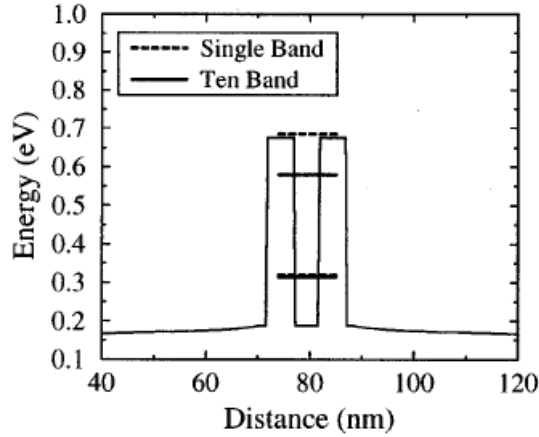
Figure 3.6: Numerically calculated resonance energies for the InGaAs/InAlAs RTD using single and full (ten) band model [24]. Figure shows energy levels of two barriers and one well in relation to the distance from top of the device.
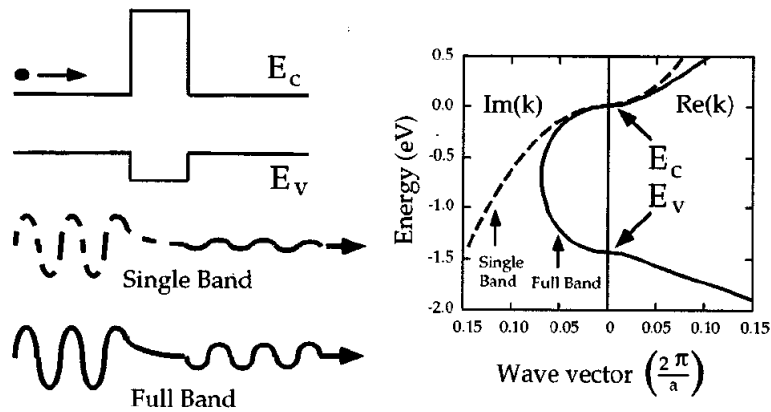

Figure 3.7: Comparison between 1-band model and full (ten) band model [24].

Using the single band model and using one effective mass and some considerations of scattering, calculations could be carried out. These calculations are very rough and fail to describe the variations of the material in the nano meter scale [25]. In heterojunctions, the bands are misaligned which makes the whole calculations more difficult. On the contrary the full band model, tries to compensate most of the deficiencies of the single band model.

The explanation of the theory behind the full band model will exceed the limits of this work. Further information could be found in [26] and [27].
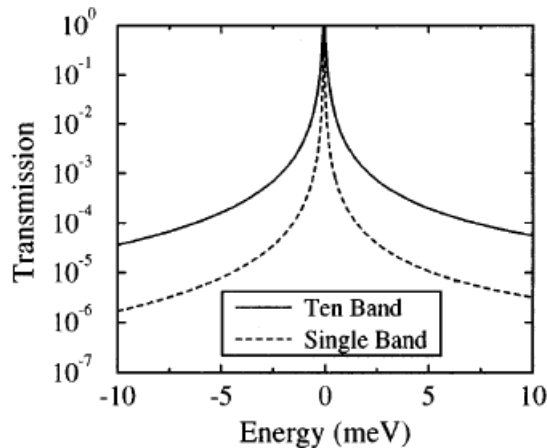
Figure 3.8: Transmission coefficient versus energy for single and full (ten) band models [24].

3.4 Modelling of Strain

Modelling of strain is needed in order to make realistic calculations in semiconductors. A mechanical force changes the positions of the atoms in a crystal. If the moved lattice points (or sites) return to their original point after removal of the mechanical force, the deformation is described as elastic [18]. If $\vec{u}$ is the displacement vector, which itself could be a function of position ($\vec{u} = \vec{u}(\vec{r})$), a second rank tensor could be defined for the displacement of the lattice

$$\epsilon_{ij} = \frac{1}{2} \left(\frac{\partial u_i}{\partial x_j} + \frac{\partial u_j}{\partial x_i} \right), i, j = 1, 2, 3 \tag{3.17}$$

where the u_1, u_2 and u_3 are the relative displacement of the lattice in the direction of the x_1, x_2 and x_3 respectively. The diagonal components of the strain tensor are called the **stretches** and the off diagonal components describe the **rotation**.

$$\epsilon = \begin{pmatrix} \epsilon_{11} & \epsilon_{12} & \epsilon_{13} \\ \epsilon_{21} & \epsilon_{22} & \epsilon_{23} \\ \epsilon_{31} & \epsilon_{32} & \epsilon_{33} \end{pmatrix} \tag{3.18}$$

If a crystal is under external forces, or is applying a force on a neighboring part, then the crystal is said to be in **stress**. The stress is usually defined as force per unit area of the crystal and is denoted as σ. Strain could be **uniaxial** or **bi-axial** depending on the existence of components in only one or two dimensions. Stress is in relation with strain components under Hooke's[13] law.

---

[13]Robert Hooke ($1635 - 1703$), English philosopher and polymath

$$\epsilon_{ij} = \sum_{k=1}^{3} \sum_{l=1}^{3} S_{ijkl} \sigma_{kl} \tag{3.19}$$

where S_{ijkl} are called *elastic compliance constants*. The equation could be rewritten as [18]:

$$\sigma_{ij} = \sum_{k=1}^{3} \sum_{l=1}^{3} C_{ijkl} \epsilon_{kl} \tag{3.20}$$

where C_{ijkl} is called *elastic stiffness constant*. In a so called Voigt's[14] notation with proper renaming of the constants, equation 3.20 could be written as:

$$\sigma_{ij} = \sum_{l=1}^{6} C_{ik} \epsilon_k \tag{3.21}$$

The C-matrix for the hexagonal structure has five components due to many symmetries instead of 36 which is the general form considering all directions. For hexagonal c-plane GaN, this would look like [18]:

$$\begin{bmatrix} \sigma_1 \\ \sigma_2 \\ \sigma_3 \\ 0 \\ 0 \\ 0 \end{bmatrix} = \begin{bmatrix} C_{11} & C_{12} & C_{13} & 0 & 0 & 0 \\ C_{12} & C_{11} & C_{13} & 0 & 0 & 0 \\ C_{13} & C_{13} & C_{33} & 0 & 0 & 0 \\ 0 & 0 & 0 & C_{44} & 0 & 0 \\ 0 & 0 & 0 & 0 & C_{44} & 0 \\ 0 & 0 & 0 & 0 & 0 & \frac{1}{2}(C_{11} - C_{12}) \end{bmatrix} \begin{bmatrix} \epsilon_1 \\ \epsilon_2 \\ \epsilon_3 \\ \epsilon_4 \\ \epsilon_5 \\ \epsilon_6 \end{bmatrix} \tag{3.22}$$

A crystal is always stable with minimum strain energy. This energy is the one required for deforming the lattice which is defined as sum of the work done by the stress components acting on the crystal [18].

Quantum wells are thin epitaxial layers which are grown between two barrier layers. If we assume that the area of the substrate is infinite, then the lattice constant of the grown crystal is forced to match that of the substrate material. This could be either in a **tensile** or in **compressive** form. Since in the growth direction, there are no forces acting upon the grown layer, a bi-axial stress exists which results in the so called **in-plane strain**, $\epsilon_\parallel$ which is calculated as

$$\epsilon_\parallel = \frac{a_0 - a_l}{a_l} \tag{3.23}$$

with a_0 and a_l being the in plane lattice constants of the substrate and epi layer respectively. If multiplied by 100, $\epsilon_\parallel$ could be written in percentage. Compred to an AlGaAs/GaAs system which has a $\epsilon_\parallel$ of smaller than 0.1%, for an AlN layer grown
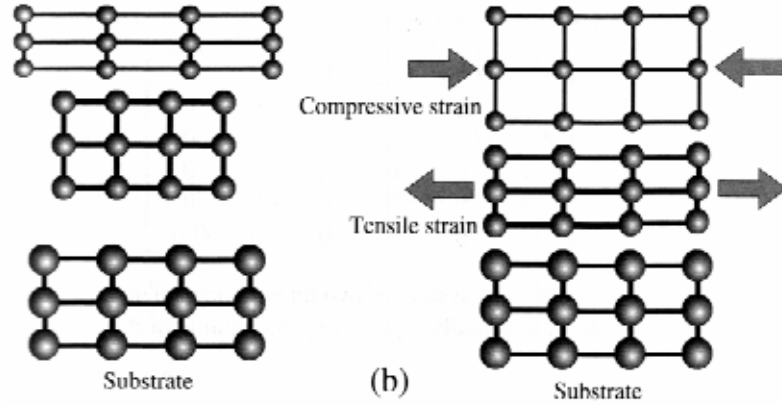
---

[14]Woldemar Voigt ($1850-1919$), German physicist

Figure 3.9: Different strain types [18]

on top of GaN where a_l is the lattice constant of AlN and a_0 the lattice constant of GaN, $\epsilon_\parallel = +2\%$ of tensile strain [18].

Due to the thickness dependency of the elastic energy, after a certain thickness (the *critical thickness*), the epilayer relaxes. This relaxation causes **defects** and **misfit dislocations**. On the other hand, a **pseudomorphic growth** is referred to a growth which allows the lattice constant of the grown layer to fully match that of the substrate. So for good quality devices, pseudomorphic growth is necessary.

An effect called **Poisson effect** causes the crystal to have also an stress component in the growth direction although initially $\sigma_3 = 0$. The compressive strain forces the in plane lattice constant to shrink, then the lattice constant in the growth direction will increase. The reverse is true for tensile strain (see Figure 3.9). The strain in the crystal also deforms the bandstructure.

By solving equation 3.22 for hexagonal wurtzite it could be concluded that

$$\epsilon_1 = \epsilon_2 = \epsilon_\parallel \tag{3.24}$$

$$\epsilon_3 = -2\frac{C_{13}}{C_{33}}\epsilon_1 \tag{3.25}$$

and in the matrix form (see equation 3.18) after application of Voigt's notation:

$$\epsilon = \begin{pmatrix} \epsilon_1 & 0 & 0 \\ 0 & \epsilon_1 & 0 \\ 0 & 0 & -2\dfrac{C_{13}}{C_{33}}\epsilon_1 \end{pmatrix} \tag{3.26}$$

where the relative change in volume could be determined by [18]:

$$\frac{dV}{V} = 2\epsilon_1 \left(1 - \frac{C_{13}}{C_{33}}\right) \tag{3.27}$$
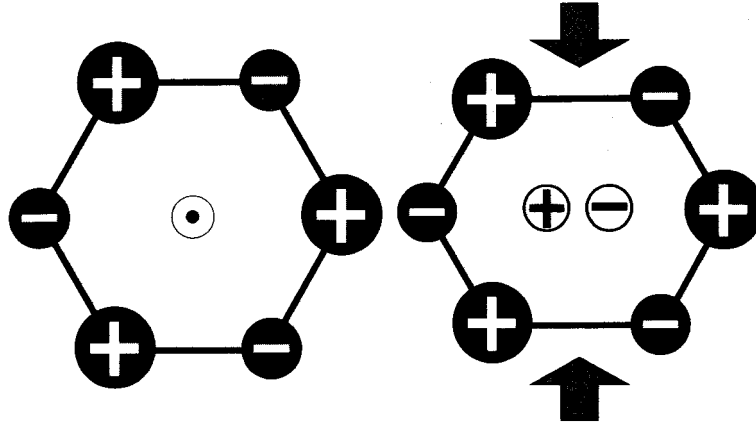
Figure 3.10: Schematic illustration of the charge separation in c-plane GaN[18]

Some semiconductors gather charge under their surface if under stress. Non compensated charge due to stress in the volume of the crystal gives rise to the **piezoelectric** effect. As depicted in Figure 3.10 like in the case of GaN, these uncompensated charges induce a global polarization vector.

The piezoelectric vector has three components P_1, P_2 in the growth plane and P_3 in the growth direction. With its relation to strain we define a 3×6 matrix of **piezoelectric moduli**, which again for the case of GaN, due to the crystal symmetry, reduces to 3.

$$
\begin{bmatrix} P_1 \\ P_2 \\ P_3 \end{bmatrix} = \begin{bmatrix} 0 & 0 & 0 & 0 & \frac{1}{2}d_{15} & 0 \\ 0 & 0 & 0 & \frac{1}{2}d_{15} & 0 & 0 \\ d_{31} & d_{31} & d_{33} & 0 & 0 & 0 \end{bmatrix} \begin{bmatrix} \sigma_1 \\ \sigma_2 \\ 0 \\ 0 \\ 0 \\ 0 \end{bmatrix} \tag{3.28}
$$

$$
P_3 = d_{31}(\sigma_1 + \sigma_2) = 2d_{31}\sigma_1 \tag{3.29}
$$

which with $\sigma_1 = \epsilon_1 \left(C_{11} + C_{12} - 2\frac{C_{13}^2}{C_{33}} \right)$ reduces to:

$$
P_3 = 2d_{31}\epsilon_1 \left(C_{11} + C_{12} - 2\frac{C_{13}^2}{C_{33}} \right) = 2\epsilon_1 \left(e_{31} - e_{33}\frac{C_{13}}{C_{33}} \right) \tag{3.30}
$$

where in the literature, the **piezoelectric constant** e is defined as

$$
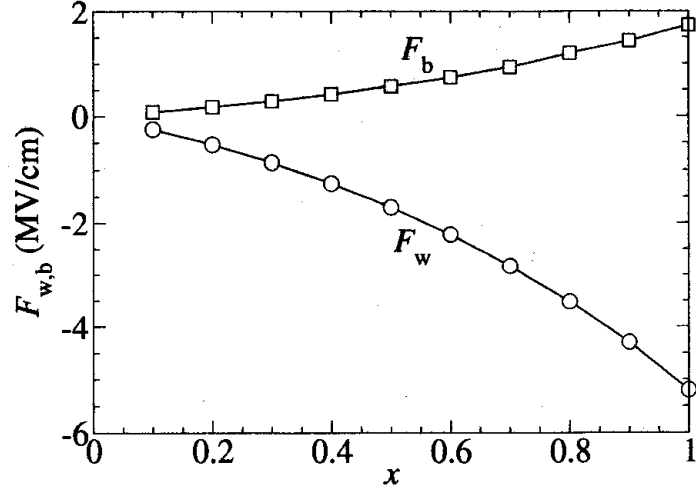e_{kl} = \sum_{j=1}^{6} e_{ik}\epsilon_k. \tag{3.31}
$$

Figure 3.11: Calculated induced piezoelectric field in GaN F_w well and two $Al_xGa_{1-x}N$ barrier layers F_b [18].

As the term $\left(C_{11} + C_{12} - 2\dfrac{C_{13}^2}{C_{33}}\right) > 0$ is always greater than zero, the sign of the polarization is determined by sign of the strain [18]. So P_3 is always positive for layers under bi-axial compressive strain, and negative under tensile strain. This was previously depicted in Figure 2.4. Equation 3.30 also indicates that a constant strain induces a constant polarization.

At the surface, a gradient of piezoelectric polarization $\vec{P}$ appears which results in a charge density

$$\rho_p = -\nabla \vec{P} \tag{3.32}$$

Imagining a system of n-layers, the resulting electric displacement vector $\vec{D}_i$ of the adjacent layers are equal.

$$\vec{D}_i = \vec{D}_{i+1} \tag{3.33}$$

with $\vec{D}_i = \varepsilon_i \vec{E}_i + \vec{P}_i$, where ε is the permittivity. For n-layers, $n-1$ linear equations could be solved with proper boundary conditions. The solution of the system could be derived for a well/barrier structure

$$F_{w,b} = \frac{(P_{b,w} - P_{w,b})l_{b,w}}{\varepsilon(l_w + l_b)} \tag{3.34}$$

with F being the magnitude of the piezoelectric field, P_w and P_b the magnitude of polarization and l_w and l_b the respective layer width. This is illustrated in Figure 3.11 for an AlGaN/GaN/AlGaN structure where the piezoelectric field in the well and barrier layers are calculated as a function of barrier layer composition. For a 20Å

AlGaN well the electric field is as large as 5MV/cm and for a 60Å well still around 1MV/cm [18].

The overall potential drop across the quantum well must be zero so the electric fields must have opposite signs which implies that the thinner the layer is, the higher the electric field will be.

$$F_w l_w + F_b l_b = 0 \tag{3.35}$$

Finally, in the quantum well, if the density of the carriers is comparable to the induced piezoelectric induced charges, then the piezoelectric field could be suppressed or **screened**, but usually the doping level in the quantum wells are not sufficient enough for this (unintentionally background doping).

4 Semiconductor-Insulator-Semiconductor Structures

Structures with a single large bandgap barrier between two lower bandgap semiconductors are often called semiconductor insulator semiconductor (SIS) because as in the case of GaN/AlN/GaN the bandgap of the barrier layer is so high that according to the definition it might as well be considered as an insulator. These structures could be used to study charge transport across a quantum barrier. Instead of showing quantum confined energy states inside a well, a single barrier is able to show tunneling effects through the barrier.

4.1 The Single Barrier

When a classical particle is incident on a potential barrier of height V, it has a 100% probability of transmission if its energy $E > V$, and while being reflected with 100% probability if $E < V$. In contrast, this is not the case in quantum mechanics due to the wave-like nature of the particles. An incident electron has a finite probability of Tunneling through a thin barrier even when $E < V$ [19].

In III-V semiconductors, a single barrier Tunneling can be formed by sandwiching a thin layer of wide bandgap material between two narrower gap materials. The transmission probability, and hence the tunneling current decreases exponentially with increasing height and width of barriers and is also dependent on the impurities in the barrier and surrounding semiconductors [19].

A measure of quantifying of charge propagation through a barrier is the **transmission coefficient** which describes the probability that *any single electron* would tunnel through the barrier. This could be mathematically formulated as [28].

$$T(E) = \frac{1}{1 + \left(\dfrac{k^2 + \kappa^2}{2k\kappa}\right)^2 sinh^2(\kappa L)}, E < V \tag{4.1}$$

where L is the barrier width and V is the barrier height and

$$k = \frac{\sqrt{2m^*E}}{\hbar} \tag{4.2}$$

$$\kappa = \frac{\sqrt{2m^*(V - E)}}{\hbar} \tag{4.3}$$

For values of E larger than the potential barrier, $\kappa \longrightarrow jk'$ ($j = \sqrt{-1}$), which means κ becomes imaginary and hence

$$T(E) = \frac{1}{1 + \left(\dfrac{k^2 - k'^2}{2kk'}\right)^2 sin^2(k'L)}, E > V \tag{4.4}$$

where

$$k' = \frac{\sqrt{2m^*(E - V)}}{\hbar}. \tag{4.5}$$

When

$$k'L = n\pi \quad , \quad n = 1, 2, 3, ... \tag{4.6}$$

there will be oscillations since the *sin* term becomes zero [18] and the $T = 1$. Putting this into equation 4.4 will imply that these resonances occur when

$$E = \frac{(n\hbar\pi)^2}{2m^*L^2} + V \tag{4.7}$$

The graphs in Figure 4.1 show the results of the calculations above for a fixed barrier height V of 100 meV in a AlGaAs/GaAs system.

Figure 4.1(a) shows that as far as $E < V$, then the thinner the barrier is, the higher is the probability of Tunneling. But above the height V, where $E > V$, the thicker the barrier is, the closer the first resonance is to the top of the barrier. This could be explained by equation 4.7 when $L \longrightarrow \infty$. For a fixed L and variable V, the first resonance always occurs at the same distance from the barrier top as depicted in Figure 4.1(b). Both Figure 4.1(a) and Figure 4.1(b) show that the squared dependence causes the peak of the transmission propability to occur at higher intervals.

4.2 Previous works on Single Barrier Structures

Bykhovski et. al. have worked on the influence of the strain-induced electric field on a c-plane single AlN barrier [29].

Herrman et. al. [6] studied the carrier transport across a single barrier. Figure 4.2 shows how barrier height is affected by the increasing barrier thickness. As depicted in Figure 4.3 the I-V curve of the structure is asymmetric due to the polarization charges.
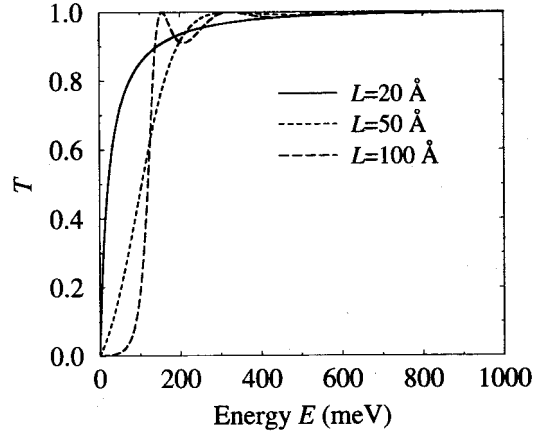
(a) Transmission coefficient as a function of energy through different barrier widths.
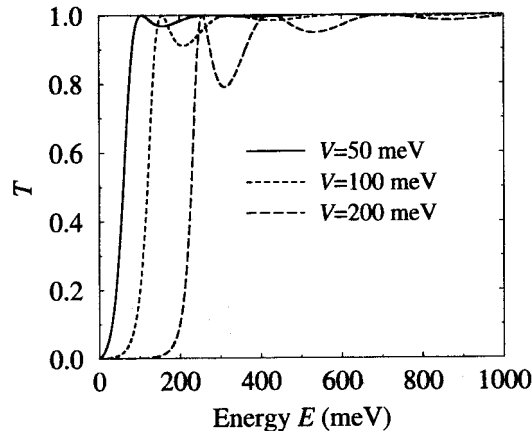
(b) Transmission coefficient as a function of energy through a 100Å barrier.

Figure 4.1: Calculated Transmission coefficient in a single barrier [18]

Keeping the transmission probabilities of Figure 4.1(a) in mind, the magnitude of the tunneling current is affected by the depletion of the emitter region due to the polarization charge accumulation, and therefore resulting in asymmetric I-V curves. They concluded that the vertical current in the single barrier structure depends on the barrier thickness and the Al composition, revealing an asymmetric dependence on the bias voltage.

Leconte et. al. studied the principles of charge distribution across a single AlN barrier [30]. They used PAMBE to grow on top of $10\mu m$ thick GaN on sapphire and 600nm n.i.d. GaN buffer. The thickness of barriers then varied between 0.5nm
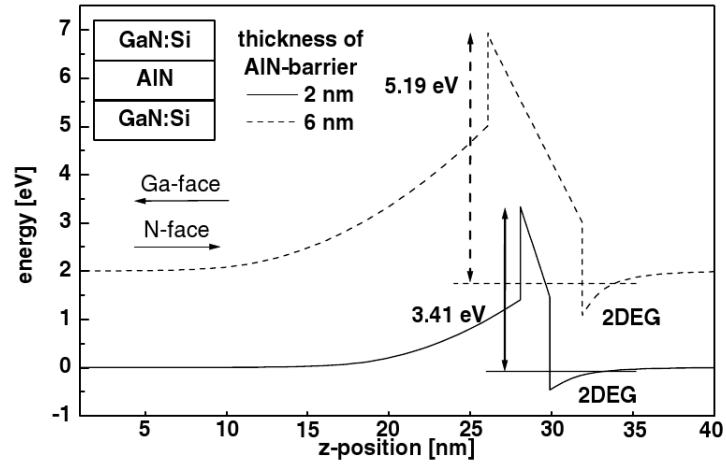
Figure 4.2: Increase of barrier height with barrier thickness due to polarization effects [6]
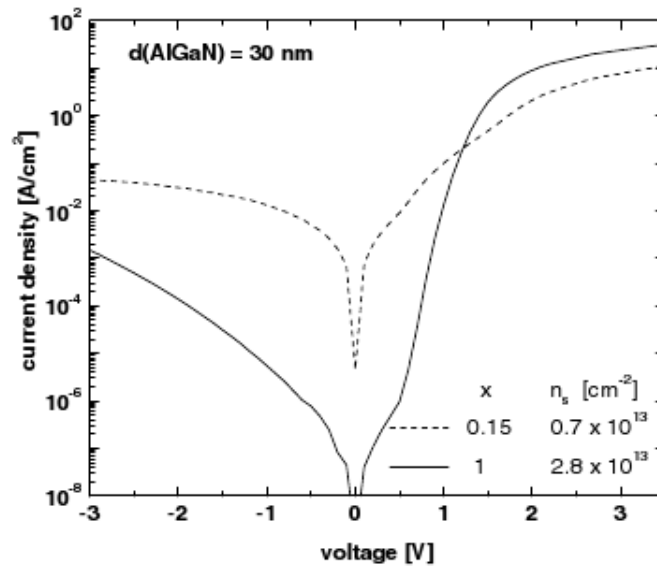
Figure 4.3: The calculated I-V curve for different sheet carrier densities [6]

and 5nm. The thickness of the cap layer was then varied between 25nm and 150nm. In their simulations with NextNano3, they assumed a GaN **residual doping** of $5 \times 10^{17} cm^{-3}$. They calculated an induced electric field of about $12 MV cm^{-1}$ in the barriers and hence a strong asymmetry. The positive polarization induced bound interface charges were partially compensated by the 2DEG, whereas the negative polarization-induced charge at the other side depletes the cap layer. With photoluminescence and capacitive measurements, they confirm the existence of the 2DEG

and depletion region. Using conductive atomic force microscopy (C-AFM) they verify the leakage current spots to be in the range of $10^7 cm^{-2}$ which was lower than the dislocation density $5 \times 10^8 cm^{-2}$. With the 5nm barrier size they observe an enhancement in the leakage current and degradation of the electrical performance, which they attribute to the relaxation of the AlN barrier layer.

In conclusion, they suggest, small diode sizes and thin barrier layers should be used for devices like RTDs.

4.3 Simulation Results

The results of the I-V and band structure simulations of both polar and non polar structures with WinGreen [31] is presented in this section. WinGreen provides a **single band** model for wurtzite GaN and features calculation of the plot of the **local density of states** (LDOS) for each corresponding bias point. A structure used for simulation in this work is shown in Table 4.1. This structure was grown with MOVPE and fabricated (sample No. HFTS158). The experimental results will be discussed in the following section. A simulation result for HFTS-158 is depicted in Figure 4.4 for a sheet carrier density[1] of $\sigma = 5.6 \times 10^{13} cm^{-2}$ which is assumed to be the fully strained AlN on GaN with spontaneous and polarization effects included [6]. The location of the 2DEG is clearly visible. Figure 4.4(a) depicts the energy band diagram of HFTS158 without bias. Due to polarization effect, 2DEG at the heterointerface can be observed. Figure 4.4(b) shows the same structure at a bias of 1.11V. It could be seen that increasing the bias voltage, increases the induced 2DEG on the right side of the barrier. Also the application of a bias voltage changes the number of carriers in the emitter side and the depletion region disappears by further increase of the bias voltage. Figure 4.5 shows the calculated local density of states across a single barrier of HFTS-158, where the transmission levels could be seen for higher bias voltages. The darker the area in the LDOS plot is, the higher is the probability of the existence of charge carriers. The 2DEG region could be seen, which is a dark area. One of the main shortcomings of the WinGreen software is the missing space charge region on the left side of the diagram.

Figure 4.6 and Figure 4.7 show the calculated simulation plot of potential and charge distribution of a 2nm single barrier and the corresponding local density of states plot. It could be seen that the thinner the barrier is, the smaller is the amount of polarization charge induced 2DEG.

---

[1]In this chapter σ denotes sheet carrier concentration unlike in the chapter 3 where it denoted the stress

4.4 Experimental Results

4.4.1 Growth

Three wafers were grown for the study of the single barrier. HFTS-158 has the structure depicted in Figure 4.8. HFTS-183 has also the same structure but with less doping on the cap layers. HFTS185 has the same structure and doping as HFTS-183 but with about 20% less barrier thickness in order to study the impact of barrier thicknesses in SIS diodes. A superlattice was used to enhance the quality of the growth as also was done by Hermann et. al. in [6]. They concluded that the superlattice reduced the dislocation density in the template. A similar structure was grown on r-plane sapphire wafer (a-plane GaN, HFTS-242). Table 4.1 summarizes the growth results for the SIS structures and Figure 4.9 shows their surface morphology. As it could be seen in Figure 4.9, the surface morphology of the r-plane sample, is much rougher compared to the c-plane growth.

4.4.2 Fabrication

The wafers were first diced and cleaned. Using AZ1518[2] they are glued to sample holders. After application of AZ4533 **photo resists** (PR) devices were patterned using ultra violet (UV) contact lithography and developed with AZ400K developer. After descumming with Oxygen plasma, dry etching was done with a **reactive ion etching** (RIE) machine from Oxford Instruments[3] for mesa isolation.

The etching depth was determined using an α-step profiler. After the removal of photo resist with PRS1000, metal contacts were deposited using **electron beam evaporation** (EBE). A multilayer of Ti/Al/Ti/Au each with 25nm/150nm/25nm/222nm layer thickness was deposited. After the deposition, the samples were soaked in Acetone overnight to facilitate easy lift-off operation. Then the samples were prepared for the thermal annealing process after which they have a typical form. Figure 4.10 shows the image of a processed diode after thermal annealing of the metal contact. In this figure the ohmic contact on top of the etched mesa is clearly visible.

The devices were fabricated in different geometries, ranging from 16 μm to 32μm. This diameter is shown as "D" in Figure 4.10.

---

[2]http://www.microchemicals.de
[3]http://www.oxford-instruments.com/

Wafer Name	Structure	Cap Doping	Results
HFTS-158	GaN 30 nm / AlN 7 nm / GaN 30 nm	Top (Emitter): $6.4 \times 10^{18} cm^{-3}$ Bottom (Collector): $3.0 \times 10^{18} cm^{-3}$	Cracked surface
HFTS-183	Same as HFTS-158	Top (Emitter): $4.2 \times 10^{18} cm^{-3}$ Bottom (Collector): $3.0 \times 10^{18} cm^{-3}$	Less surface cracks than HFTS-158
HFTS-185	GaN 30 nm / AlN 6 nm / GaN 30 nm	Same as HFTS-183 but with 20% less barrier thickness	Best surface morphology
HFTS-242	Same as HFTS-158	Same as HFTS-185	Extremely rough surface

Table 4.1: Wafers grown for SIS Structures

4.5 Measurements

4.5.1 Transmission Line Measurements

Using the available square patterns on top of each sample after thermal annealing, transmission line measurements were carried out. The TLM patterns consisted of 7 square pads each $50\mu m$ by $50\mu m$. The distances between these pads were 2, 3, 6, 9, 12 and 15 microns. Contact resistance R_C, sheet resistance R_S and specific contact resistance R_{SC} could be measured as listed in Table 4.2. For these calculations a parasitic resistance of $R_P = 10\Omega$ was assumed.

Wafer Name	$R_C[\Omega mm]$	$R_S[\Omega/\square]$	$R_{SC}[\Omega cm^2]$
HFTS-158	1.9×10^{-3}e-3	0.378	1.94×10^{-7}
HFTS-183	2.3×10^{-3}	1.02	1.06×10^{-7}
HFTS-185	1.2×10^{-3}	0.65	4.62×10^{-7}

Table 4.2: Transmission line measurements for single barrier wafers.

4.5.2 Current-Voltage

DC measurements of the samples confirm the asymmetry of the I-V curve of the devices. The measured I-V curve is depicted in Figure 4.11.

By calculating the ratio of the backward current to the forward current, one could see how asymmetric these graphs are. This is depicted in Figure 4.12.

Figure 4.13 shows the measured I-V curve for the non polar sample. As it could be seen in Figure 4.14 these curves are much more symmetric compared to the c-plane samples.

Figure 4.15 once again shows I-V measurement of HFTS-158 and a simulated I-V of the same structure. The simulated I-V has a current magnitude which is much higher due to the shortcomings of the single band model calculations. So the amplitude of the simulated data has been normalized to the real measurement in order to be able to compare the shapes. The shapes are roughly the same, but the simulation models still need improvements.
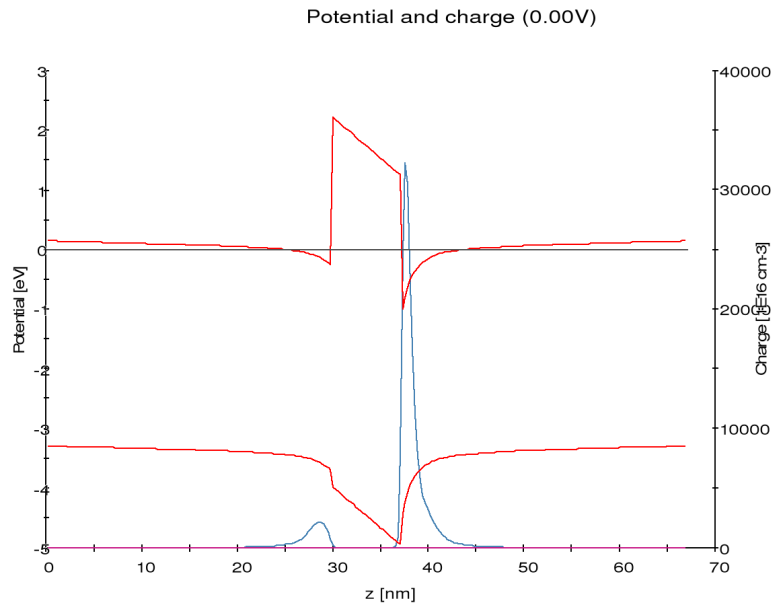
Potential and charge (0.00V)

WinGreen - F:\Sanjari\Work_WinGreen\HFTS_158_2.inp (19 January 2009, 14:30)

(a) $V_B = 0V$

Potential and charge (1.11V)
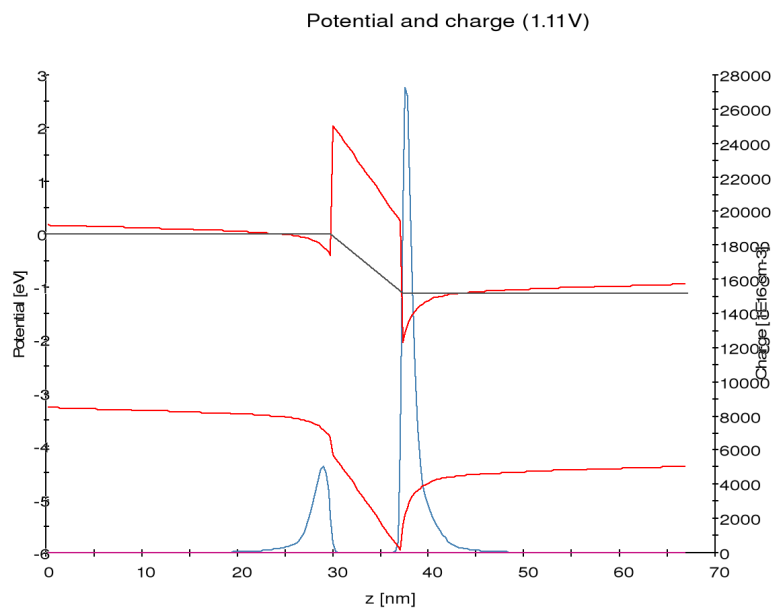
WinGreen - F:\Sanjari\Work_WinGreen\HFTS_158_2.inp (19 January 2009, 14:30)
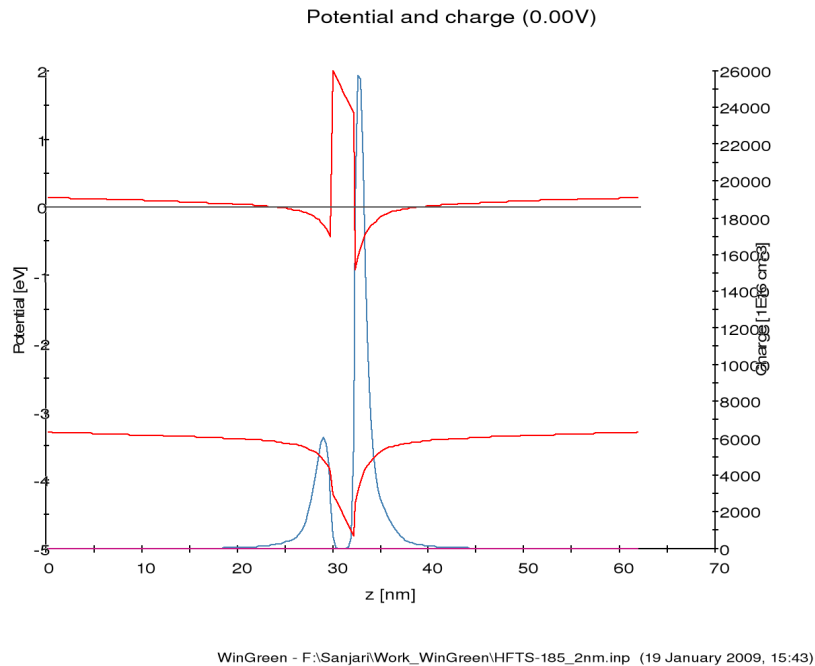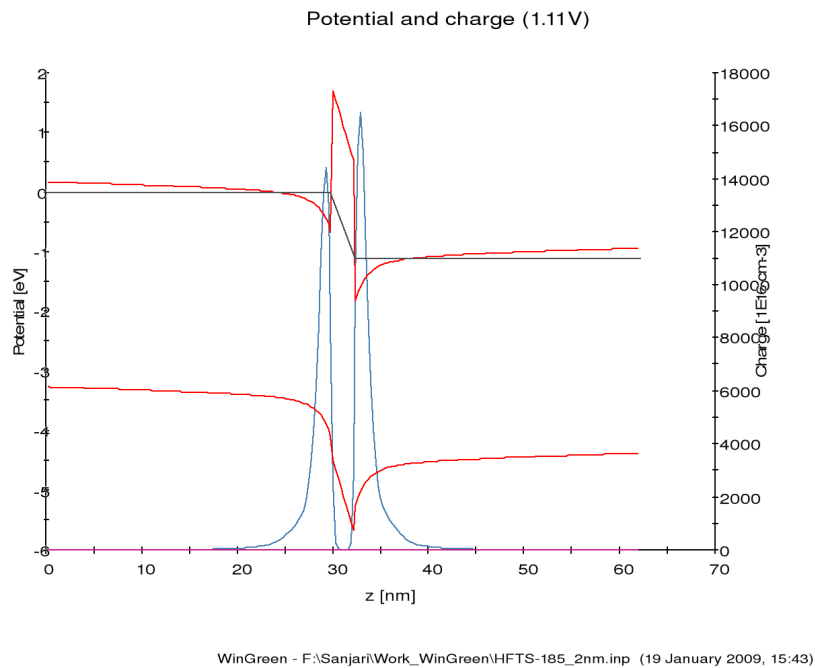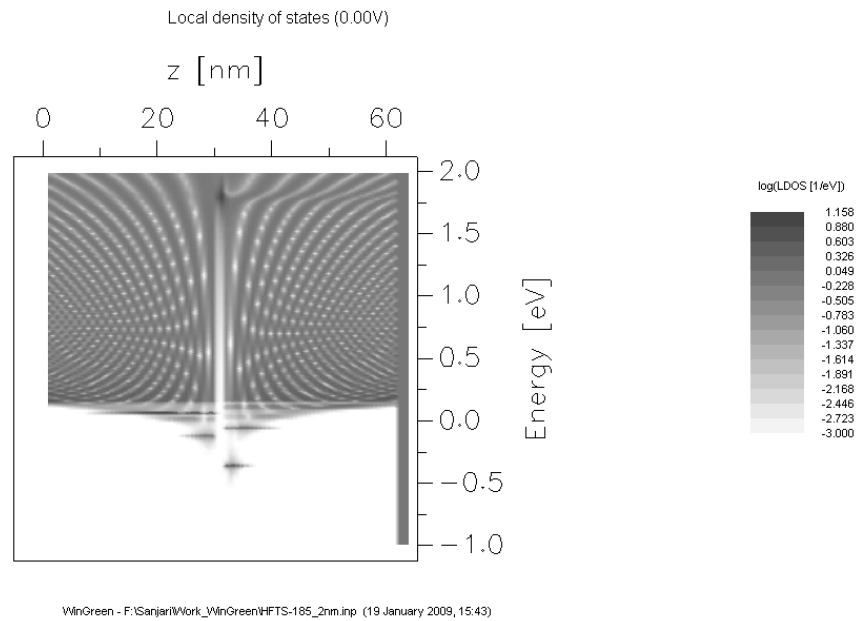
(b) $V_B = 1.11V$

Figure 4.4: A simulation plot of Potential and charge distribution on HFTS-158
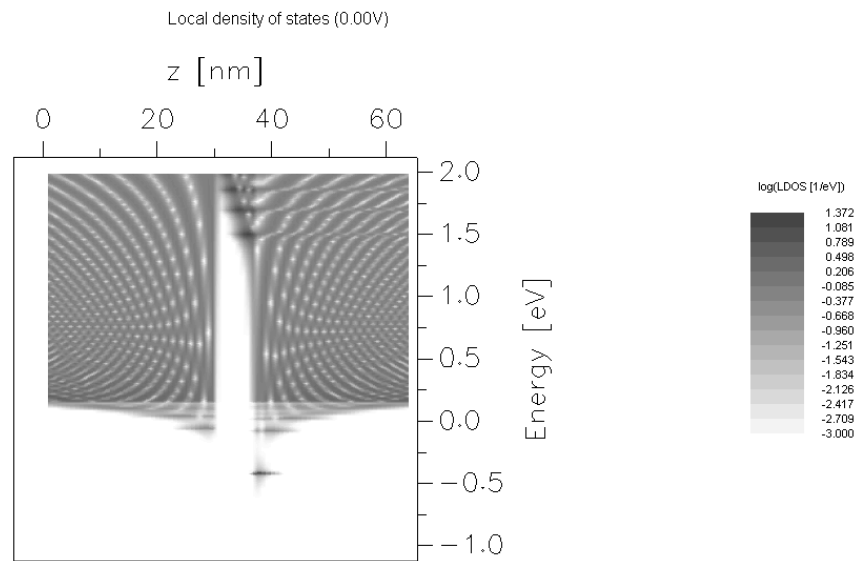
49

Local density of states (0.00V)

z [nm]

WinGreen - F:\Sanjari\Work_WinGreen\HFTS_158_2.inp (19 January 2009, 14:30)

(a) $V_B = 0V$

Local density of states (1.11V)

z [nm]
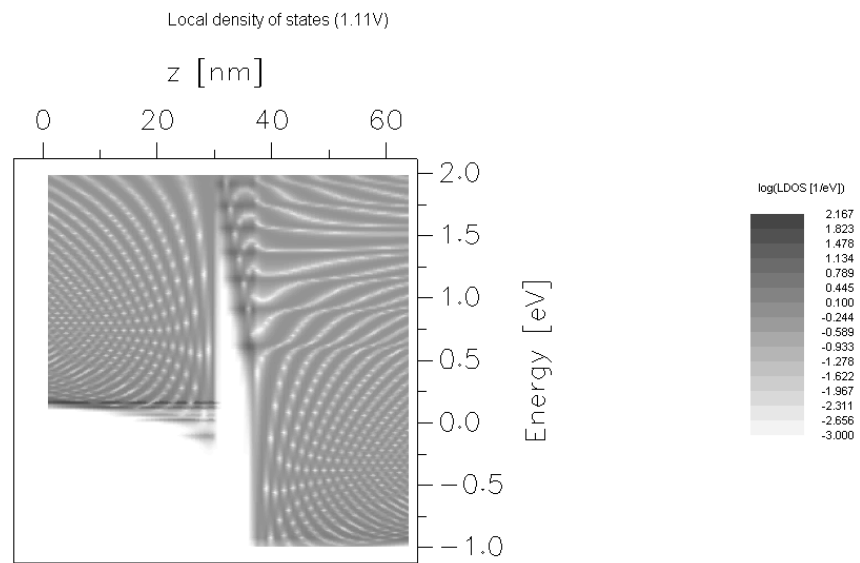
WinGreen - F:\Sanjari\Work_WinGreen\HFTS_158_2.inp (19 January 2009, 14:30)

(b) $V_B = 1.11V$

Figure 4.5: A simulation plot of local density of states on HFTS-158

Potential and charge (0.00V)

WinGreen - F:\Sanjari\Work_WinGreen\HFTS-185_2nm.inp (19 January 2009, 15:43)

(a) $V_B = 0V$

Potential and charge (1.11V)

WinGreen - F:\Sanjari\Work_WinGreen\HFTS-185_2nm.inp (19 January 2009, 15:43)

(b) $V_B = 1.11V$

Figure 4.6: A simulation plot of Potential and charge distribution on a 2nm single barrier

Local density of states (0.00V)

(a) $V_B = 0V$

Local density of states (1.11V)
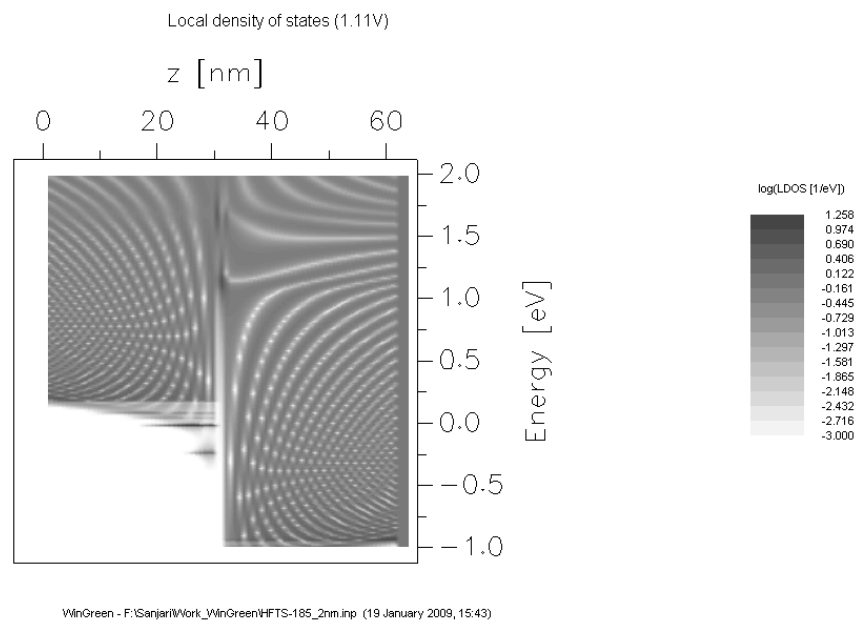
(b) $V_B = 1.11V$

Figure 4.7: A simulation plot of local density of states on the same structure as HFTS-158 but with a 2nm barrier

Emitter
Contact
Ti 225nm (bottom)
Al 1480nm
Ti 225nm
Au 2222nm (Top most)

155 nm GaN:Si
6.4e18 cm-3
10 sccm Silane

30nm GaN u.i.d

7-8nm AlN u.i.d

Barrier

30nm GaN u.i.d

550nm GaN:Si
3e18 cm-3
5 sccm Silane

Collector
Contact
Ti 225nm (bottom)
Al 1480nm
Ti 225nm
Au 2222nm (Top most)

7-8nm AlN
(gray)

10nm GaN:Si
(white)
5e17 cm-3
0.1 sccm

450nm GaN u.i.d

1.5um GaN u.i.d

Spacer

28 nm GaN

~430um Sapphire

Nucleation

Figure 4.8: Growth structure of HFTS-158 (not to scale)

(a) Surface of HFTS-158

(b) Surface of HFTS-183

(c) Surface of HFTS-185

(d) Surface of HFTS-242
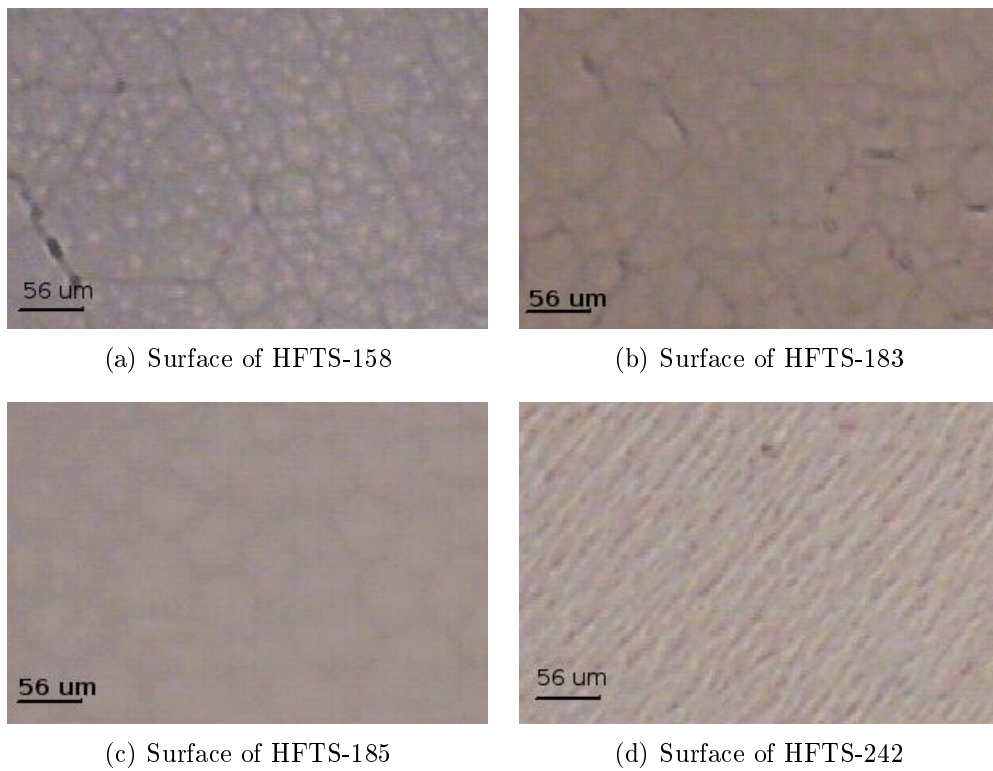
Figure 4.9: Surface morphology of the grown for single barrier structure wafers

28 um

(a) 10x zoom

D

7.8 um
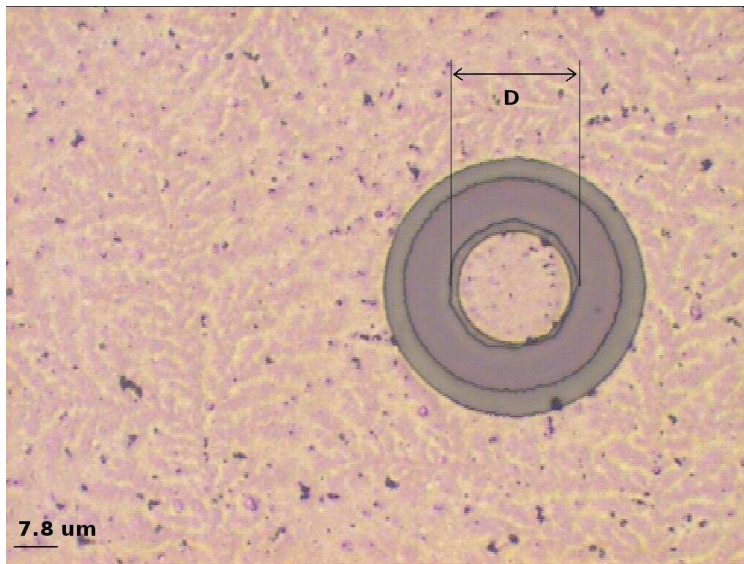
(b) 50x zoom

Figure 4.10: A fabricated diode on HFTS-183
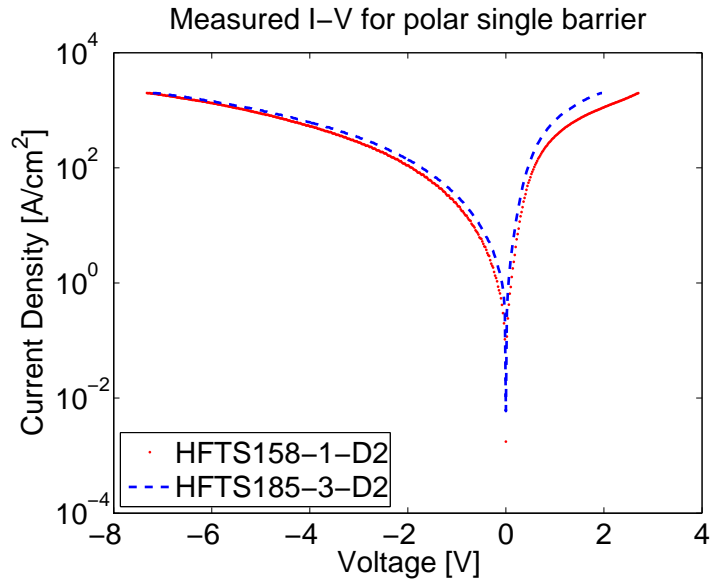
Figure 4.11: Measured I-V curve for samples HFTS-158, HFTS-183 and HFTS-183
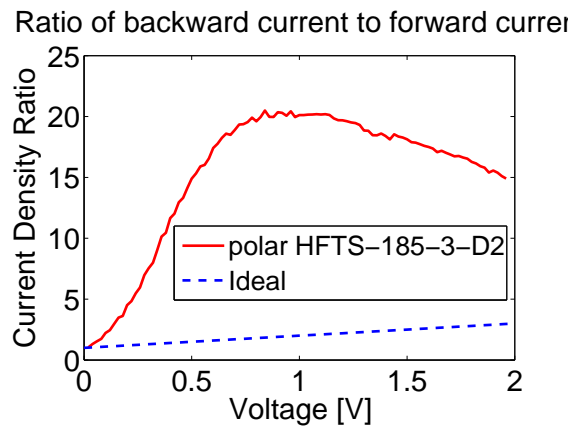
Figure 4.12: Difference in the measured forward and backward voltages for c-plane sample
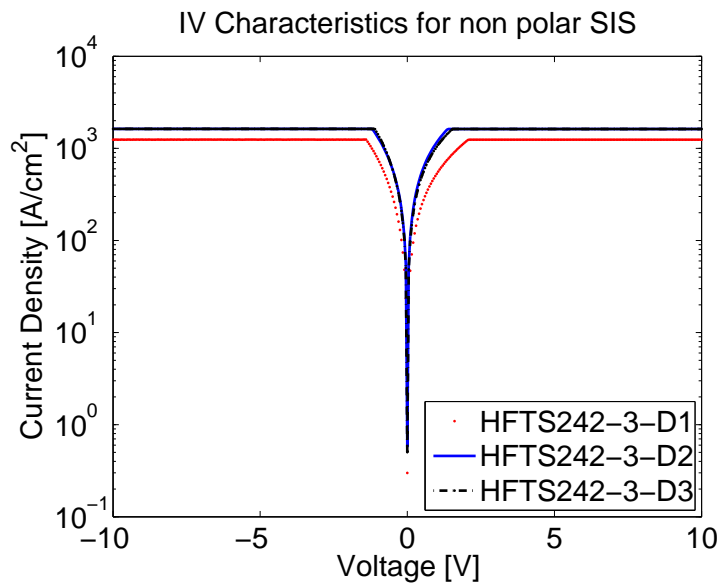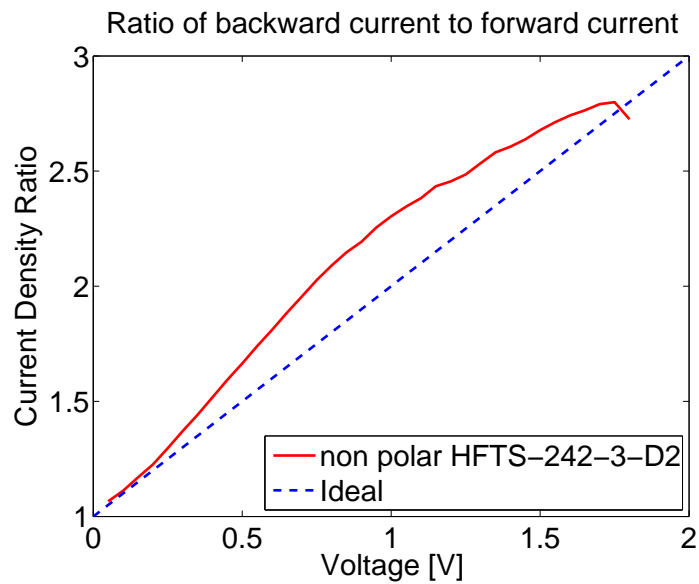
Figure 4.13: Measured I-V curve for sample HFTS-242

Figure 4.14: Difference in the measured forward and backward voltages for non polar sample HFTS-242
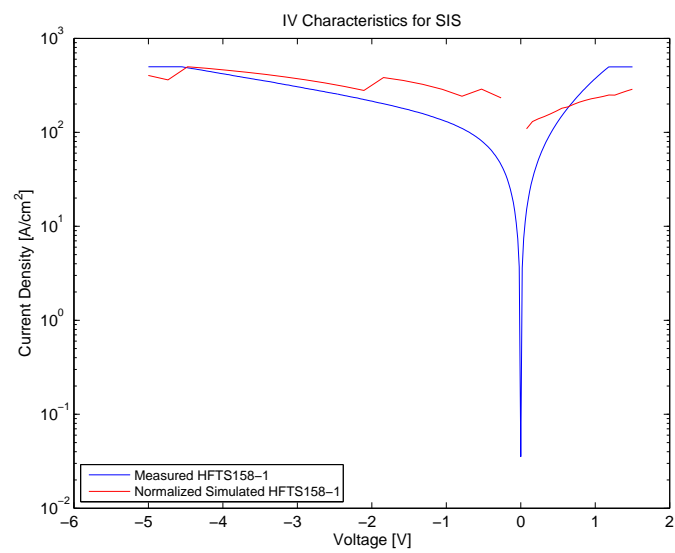
Figure 4.15: The comparison between the simulated and measured I-V for the HFTS-158

5 Double Barrier Resonant Tunneling Diodes

5.1 The Double Barrier

In a double barrier structure, two barriers are separated by a thin narrow bandgap semiconductor layer. If the barriers were wide enough, we can clearly recognize the central region as a quantum well with a set of confined state energies E_1, E_2, etc. Even with narrow barriers there will be resonant states in the well region. The Tunneling probability through the double barrier structure as a function of incident energy, E can be calculated. Except at the positions of confined states, the tunneling rate decreases with increasing barrier height, except that near the confined state energies, $E1$, etc.

Datta has deduced the transmission coefficient across the double barrier structure [32] for the case of symmetric barriers. After writing a set of equations for each section of the device, the whole equation system could be simultaneously solved to get $T(E)$ which is presented in the graph of Figure 5.1(a) for a barrier height of 100meV and a barrier thickness of 100Å. In this figure, L_2 is the distance between the barriers and the effective masses were taken to be equal to the balk Γ valley electron mass of $0.067m_0$ in GaAs system.

The main difference between the double barrier and the single barrier case is the existence of the Dirac terms, i.e. peaks in the function in the case of $E < V$. This means that the transmission coefficient becomes unity for certain energy levels. These are *non-stationary* states where electrons and holes scatter to lower energies outside of the barrier. These energies are also called *quasi-bound* states, since they resemble the bound states inside the regular quantum well [18].

Figure 5.1(a) also shows that increasing barrier thickness decreases T apart from the energies where T is at resonance. Another almost intuitive consequence (which is shown in Figure 5.1(b)) is, that increasing the barrier height by adding more Aluminum in the alloy, would increase the resonance energies due to confinement effects. Eventually (higher) quasi-bound states also appear.

Since the transmission coefficient is not a measurable quantity, the usual way is to measure the current-voltage (I-V) characteristics of the device. A schematic representation of such a resulting I-V curve is shown in Figure 5.3, where three different regions could be identified.

(a) A 100meV barrier.

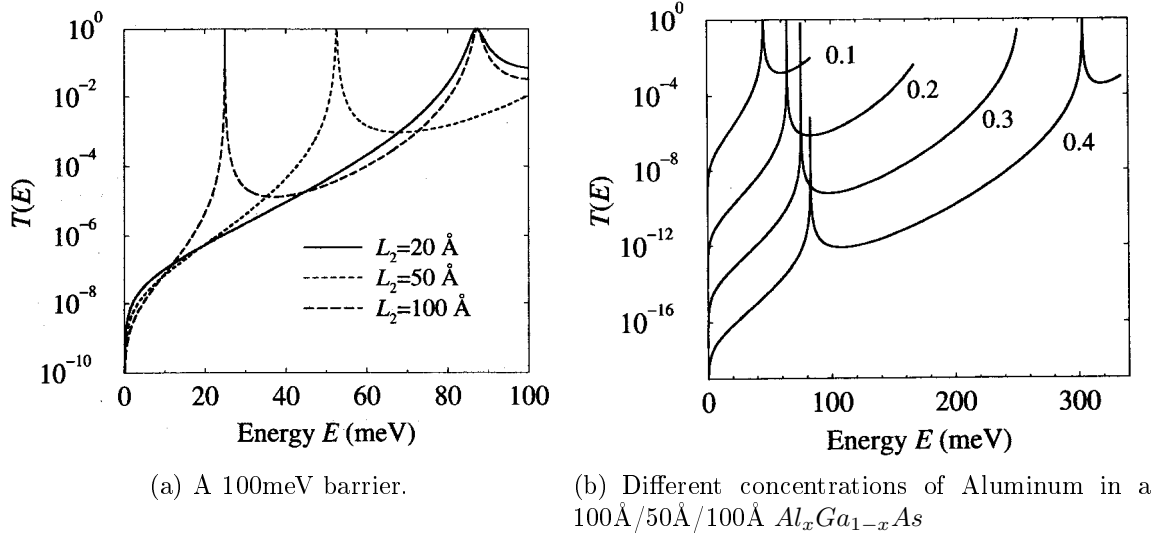(b) Different concentrations of Aluminum in a 100Å/50Å/100Å $Al_xGa_{1-x}As$

Figure 5.1: Transmission coefficient as a function of energy [18]

Electrons that exist in the lattice, no matter what their origin is (through doping or intrinsic), are incident on one side of the structure when an electric field is applied. They have an energy distribution since not all of them have the same energy and momentum which is described by the Fermi-Dirac distribution. Carriers with same energy as the resonance energy can pass through the structure without any hindrance which is the definition of the **resonant tunneling**. This is shown in Figure 5.2. As the electric field increases, the number of carriers with resonance energy increases. The peak of the number of carriers is reached when the Fermi level of the semiconductor on the incident side[1] is brought into alignment with the resonance energy [18]. Increasing electric field, moves up the bottom of the bulk conduction band relative to the center of the double barrier structure by ΔE, which is given by:

$$\Delta E = eF(L_1 + \frac{L_2}{2}) \tag{5.1}$$

Where F is the field as shown in Figure 5.3 in region I. After the peak is reached, the energy levels fall off resonance and the negative region happens where less and less electrons have the same energy as the resonance, although the applied electric field is still growing. As the energy distribution continues to shrink, the curve shows the so called **valley current** as shown in Figure 5.3 in region II. The valley current would be zero in the absolute temperature (0°K).

Higher electric fields accelerate more charge carriers with energies higher than the barrier and shoot them over it. Then the current increases again as shown schematically in Figure 5.3 in region III.

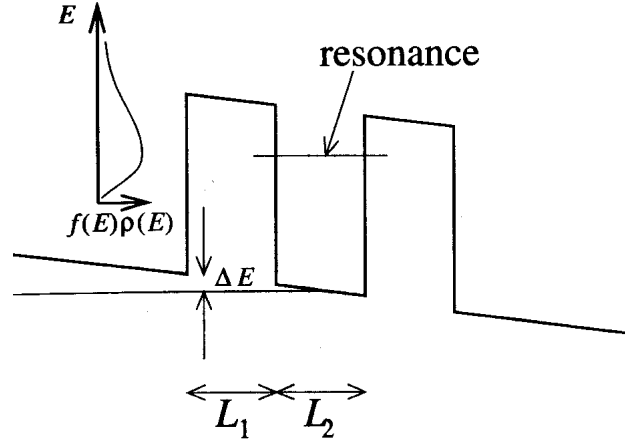[1]Sometimes called the **emitter** in the literature.

Figure 5.2: Simple model of current flow through a double barrier structure [18].
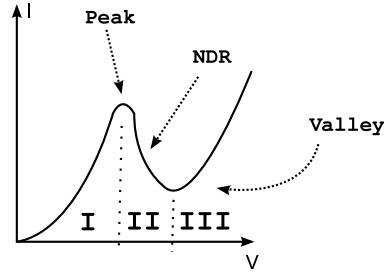

Figure 5.3: The schematic current-voltage characteristics of NDR region [19].

The conductivity decreases with the increasing temperature, as shown in equation 5.2,

$$f(E) = \frac{1}{e^{(E-E_f)/kT} + 1} \tag{5.2}$$

where f is the probability that a given available energy state will be occupied at a certain temperature, k the Boltzmann constant, T the temperature and E_f the quasi-Fermi level. As the temperature decreases, since the number of electrons which posses the resonant energy are reduced which means, the width of the distribution is reduced so the current voltage curve peak width is also reduced. This is shown in Figure 5.4. In this figure, the non zero current is due to the simplicity of the chosen model [18].

This effect can be used to achieve **negative differential resistance** (NDR). The double barrier structure is designed with n-doped layers on either side of the undoped double barrier region so that a good transition to the ohmic contacts are guaranteed. For zero bias, electrons incident for example from left are off-resonance. When a positive voltage is applied, much of the applied bias is dropped across the undoped
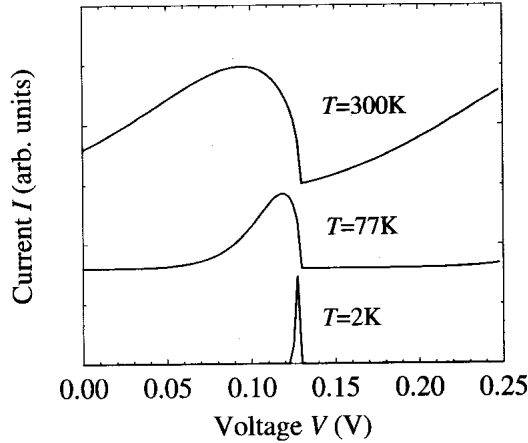
Figure 5.4: Temperature dependent current-voltage curve for the 100Å $Al_{0.2}Ga_{0.8}As$/50Å $GaAs$/100Å $Al_{0.2}Ga_{0.8}As$ of the Figure 5.1(b) [18]

barrier region, so that resonant Tunneling becomes possible, leading to sharp increase in current. With further applied bias, the incident resonant moves off-resonance, and the Tunneling and hence the current reduces with increasing voltage, giving a NDR region [19]. In this case the central resonance will disappear under the sea of electrons i.e. under the conduction band edge. Figure 5.5 shows the above process schematically. Assuming the barrier is infinitely high, then infinite number of NDR regions would appear, but since usually the electric field causes an increase in the carrier to much higher values than the barrier height, the curve never comes down a second time.

In general, calculations could be extended to asymmetric barriers with different barrier heights. The study of this case could be seen in [28]. Asymmetric barrier heights could be achieved by different mole fractions of each barrier layer. In this case, the transmission probability will be reduced, because the solutions of the system of equations will change, meaning fewer alignments are possible through the whole system of barriers and wells. The best transmission occurs when the barriers are perfectly symmetric.

Resonant tunneling can occur not only over two barriers. The general solutions of a **multiple quantum well** device will also contain resonant levels which may be completely different from the solutions of a double barrier system.
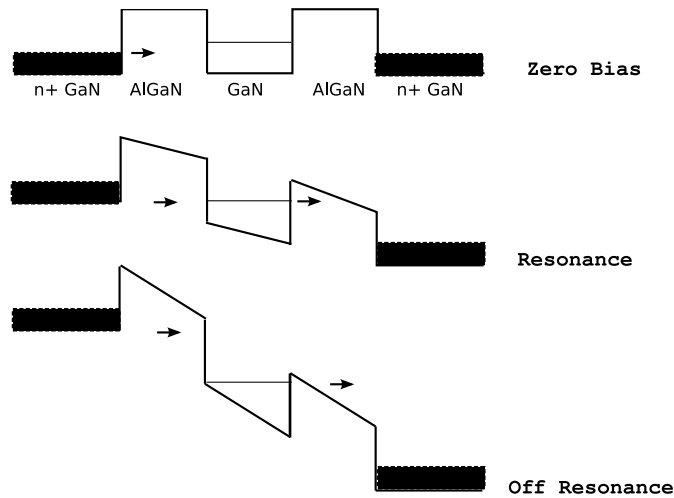
Figure 5.5: The negative resistance in a double barrier structure, after [19]. Arrows show direction of electron transport

5.2 Applications of RTDs in Signal generation and Amplification

The NDR properties of the RTDs are specially interesting for applications concerning multiply-valued logic and sub-millimeter wave generation. For the generation of millimeter waves RTDs could be used as oscillators, with different application fields like radio astronomy, remote sensing of atmosphere, material research spectroscopy, plasma diagnostic experiments and radar imaging techniques [33].

The small size of RTD based oscillators is of interest for space-born applications compared to the bulky setup of the Gunn diode oscillators. [33]. Resonant Tunneling effect is also used in quantum cascade laser devices [19].

Double barrier resonant tunneling structures are also used in resonant tunneling transistors where the gates are placed to the sides of the structure [34]. These devices are sometimes called resonant tunneling hot electron transistors (RHET) [35]. Other applications in digital circuits could be found in [36].

5.3 Previous works on RTDs

Experimental results on GaN RTDs have rarely been successful. Still the procedures are not reproducible. In 2002, Kikuchi et. al. used RF-plasma assisted MBE (PAMBE) to grow a structure which consists of a 3 monolayer (ML) GaN well between two 4 ML of AlN barriers. Cap layers were n-type GaN between $N = 8 \times 10^{18} cm^{-3}$ and $1 \times 10^{19} cm^{-3}$ [37].

Figure 5.6 shows the I-V curve presented by Kikuchi et. al. They observed an
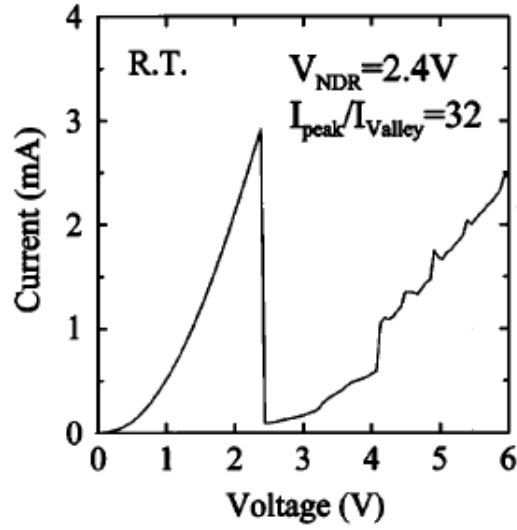
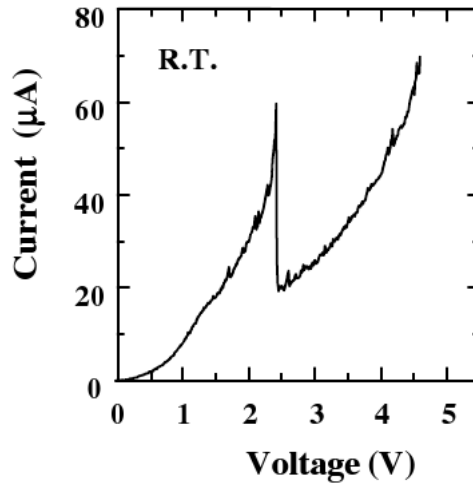Figure 5.6: Measured I-V curve of the RTD by Kikuchi et. al. [37] and [38].

Figure 5.7: Measured I-V curve of the RTD by Kishino et. al. [40].

NDR at the bias voltage of 2.4V, a peak to valley current ratio (PVCR) of about 32 at a peak current density of $180Acm^{-2}$. In this experiment a positive voltage sweep was applied. In a following paper [38] and a comment by Belayev et. al. it was also discussed that the measurements are always dependent on the sweep direction. [39].

In 2002 Kishino et. al. fabricated a 4 ML AlN/ 3 ML GaN /4 ML AlN with a cap doping of $N = 8 \times 10^{17}cm^{-3}$ [40] using RF-MBE. They measured a 60 peak current at 2.4V with a PVCR of 3.1 corresponding to a current density of $930mAcm^{-2}$ which is shown in Figure 5.7.

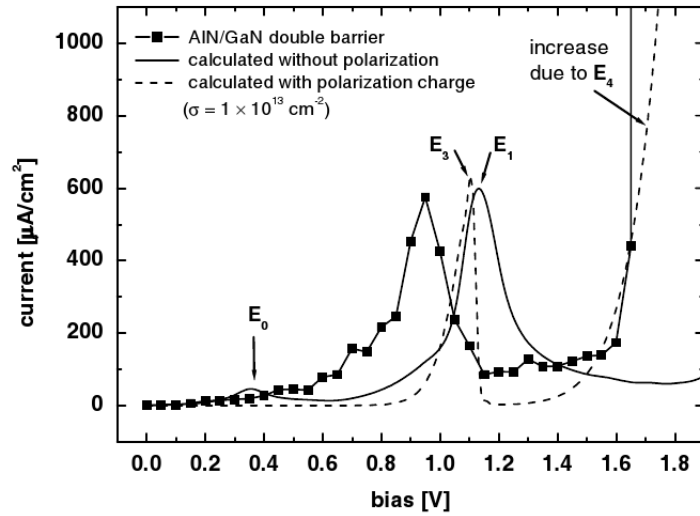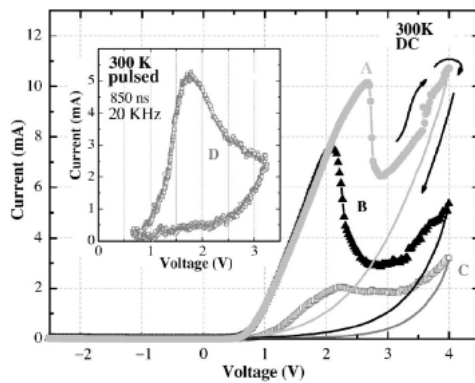Figure 5.8: Measured I-V curve of the RTD by Foxon et. al. [41].

In 2003 Foxon et. al. have reported current-voltage instabilities in a 2nm Al/2nm GaN/1nm AlN structure using molecular beam epitaxy [41]. The 1nm AlN layer was the upper barrier in the structure. Diodes had a lateral diameter of $100\mu m$ and were grown on MOVPE grown GaN templates. At the time of measurement, the forward bias was applied to the top contact, therefore injecting electrons from bottom. A current peak was visible at the initial reverse bias at -6V with a PVCR of about 4 which is shown in Figure 5.8.

They confirmed reduction of the peak amplitude after each subsequent measurement, and the current at any given voltage was found to be dependent on the direction of the sweep. Moreover they found persistant disappearance of the current peak in the opposite (negative) sweep direction. This was believed to be due to bias dependent trapping of tunneling electrons in and around the quantum well is responsible for this behavior, since the I-V curve shows weak dependence to magnetic field and the current instabilities increase in lower temperatures. A large concentration of interfacial and dislocation states specific to nitride heterostructures mask the electron tunneling behavior.

In 2004 Hermann et. al. have reported an AlN/GaN RTD where defects in the AlN barrier short circuited the tunneling current [6]. The structure of the RTD was 6nm GaN well sandwiched between two 3nm AlN barrier, then 30nm of undoped GaN Spacer on each side. For the cladding layers they used n-type GaN with $N = 8 \times 10^{18} cm^{-3}$. Figure 5.9 is the I-V curve measured by Hermann et. al.

They observed an NDR with the peak voltage at the bias of 1V, a peak to valley current ratio (PVCR) of about 8.3 at $600\mu Acm^{-2}$. They confirmed that the polarization charges largely shift the I-V curve, but still the leakage currents were the major problems and that the quality of charge transfer is very much dependent on material quality. They concluded that the optimized MBE growth temperature for the AlN barriers is $720°C$.

In 2006 Golka et. al. used low dislocation density templates with sophisticated fabrication process to produce single diodes of down to $6\mu m$ diameter in a 2nm

Figure 5.9: Measured I-V curve of the RTD by Hermann et. al. [6].

Figure 5.10: Measured I-V curve of the RTD by Golka et. al. [42].

$Al_{0.7}Ga_{0.3}N/2nmGaN/2nmAl_{0.7}Ga_{0.3}N$ system [42]. They used a cap doping of $N = 5 \times 10^{18}cm^{-3}$. They used SiO_2 passivation of the surface of the device, making it possible to reduce the lateral size of the diodes, cover them with the passivation layer, then connect a large pad of metal contact over the passivation layer up to the top contact of the diode. Most of their devices show exponential background, but they could differentiate between two groups of sharp NDR and smooth NDR. As other groups found out, the sharp NDRs are random in their peak voltage and their drop in current is unrealistically sharp so that these have been ignored. Figure 5.11 shows the measured smooth NDRs (F1 to F5) and the sharp NDRs (G1 and G2).

They also confirm the change in the retrace of the measurement. After each resonant peak, the peak is shifted to higher voltages. They find that the envelope of these traces show an original NDR, shown as dashed lines in Figure 5.11. Figure 5.10
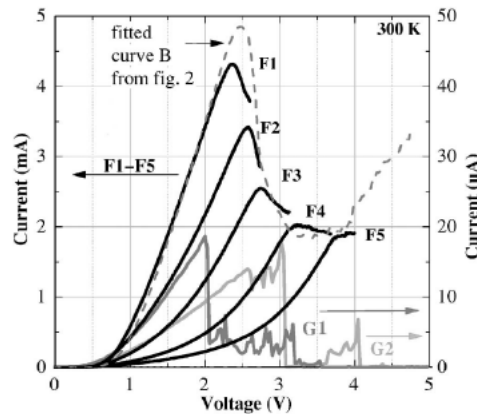
Figure 5.11: Measured retrace of the I-V curve of the RTD by Golka et. al. [42].
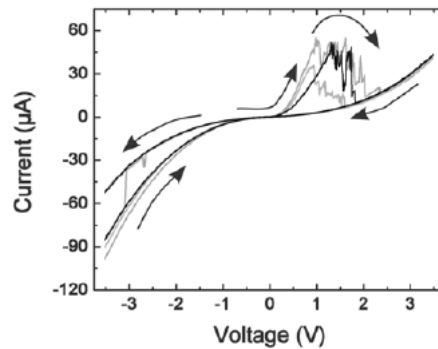
Figure 5.12: Measured I-V curve of the RTD by Leconte et. al. [43].

shows pulse measurements (1.7%, 850ns, 20KHz) versus continuous time measurements. Restoring charge traps are achieved by thermal treatment.

In 2008 Leconte et. al. fabricate $6\mu m$ mesas in a 0.5nm AlN/0.5nm GaN/0.5nm AlN system [43]. They also measure samples with non-stable high current level, and others with reproducible low current level. An NDR could be seen only by applying positive sweep at 1.5V with a PVCR of 3.2. Figure 5.12 shows the I-V curve of the stable devices. In high current state the current doesn't reduce with increasing well thickness, but in the low current state, it does, where if could be considered as an indication of tunneling.

They conclude that the existing bi-stability and the abrupt change from high current to low current state could be attributed to charge trappings. In a separate work [30], Leconte et. al. show that dislocation densities of their sample is about $10^7 cm^{-2}$ where they could expect an average of 3 leakage paths per mesa.

During the present study, there are no works known to the author describing the process of non-polar RTDs. Table 5.2 lists the summary of the works done on DB-
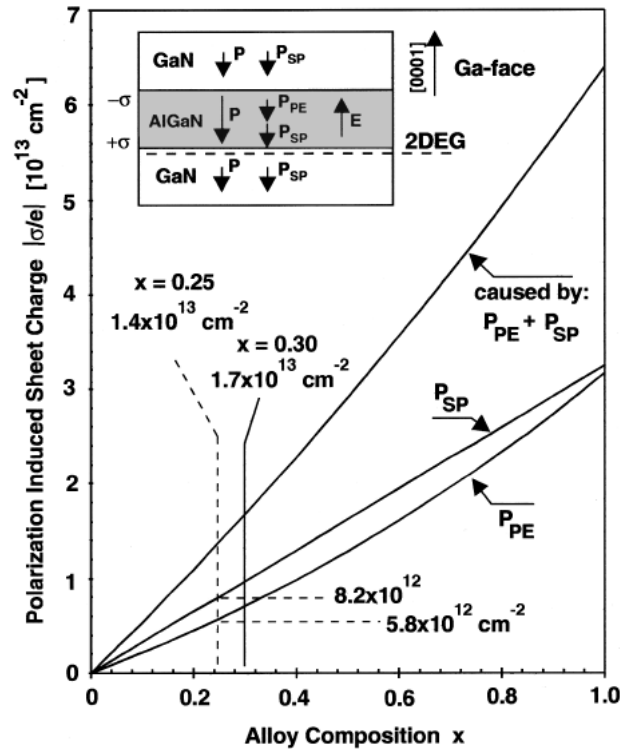
Figure 5.13: Calculated polarization induced charges vs. alloy composition [12].

RTD structures.

5.4 Simulation Results

In this section the simulation results of the double barrier RTD with WinGreen [31] software are presented. By controlling the layer structure, polar and non-polar structures were imitated and their I-V curve were compared. AlGaN and AlN were considered as a barrier layers. In the case of AlGaN layer, Al composition was 30%. In these simulations, a sheet carrier concentration of $\sigma = 5.6 \times 10^{13} cm^{-2}$[2] was assumed which corresponds to a fully strained AlN layer [12]. For the 30% AlGaN, the value of $\sigma = 1.7 \times 10^{13} cm^{-2}$ was used. This has been calculated by Ambacher et. al. in [12] which could be seen in Figure 5.13.

In the simulation software (WinGreen), this layer could be added as one monolayer of AlN (or AlGaN respectively) below the barrier. In all these simulations, the simulated barrier-well-barrier layer structure is given in the caption of each graph, plus

---

[2]In this chapter σ denotes sheet carrier concentration unlike in the chapter 3 where it denoted the stress

an additional 10nm doped GaN:Si with $N_S = 10^{18} cm^{-3}$ layer on each side as ohmic contact.

Figure 5.14(a) shows the simulation results of the band structure of a c-plane DBRTD, with a well width of 4nm and barrier width of 4nm in zero bias and 2.31V and Figure 5.15 shows the corresponding local density of states plots. Here one could see the effect of the self-consistent calculations which incorporate the space charge due to doping differences where the plot of band structure moves upward int the undoped **cladding** regions, as if the barriers are put on top of a hill[3]. Dark horizontal lines in the LDOS plot correspond to the calculated quasi-bound resonance states. As it could be seen, the applied voltage pulls down the resonance levels and the well itself.

Just as a comparison, Figure 5.16 shows a double barrier with the same layer structure but in a GaAs/AlGaAs system and incorporating the ten band nearest neighbor model. One can clearly see the difference in charge distribution in zero and biased conditions due to the lack of polarization effects.

Simulation results of DBRTD with polarization charges conclude as follows:

- The graphs in Figures 5.17, 5.18, 5.19 and 5.20 suggest that use of AlN is preferable to alloyed material i.e. AlGaN, because of higher resulting peak to valley ratio.

- The above mentioned graphs also suggest that generally thin layers as barriers should be used. Thin barriers enhance the current trough them. The number of quasi-bound states become more discrete and higher in energy level as compared to thick barriers.

- The graphs in Figures 5.21 and 5.22 suggest that the optimum barrier is about **3nm** among others which are larger.

- The graph in Figure 5.23 shows that well thickness reduces current flowing through the thickness. Inversely it could be understood that the thinner the barrier thickness, the larger the current density through the barrier will be. This current will saturate as the Figure 5.23 suggests, so in the design rules, the conditions for the well thickness could be relaxed.

To fulfill the resonance condition, the position of the a discrete energy level in the quantum well has to move below the Fermi level in the emitter region due to the application of a forward bias.

In the following, simulations were carried out for the same structures as in the polar structures, but without any sheet carrier concentration, i.e. $\sigma = 0$ to resemble the lack of polarization induced interface charges.

Figure 5.24(a) shows the simulation results of the band structure of the non polar DBRTD in zero bias and 1.92V, while Figure 5.25 shows the corresponding local

---

[3]Please refer to the documentation of the simulator in [44]

density of states plots. Here one could see what happens if the ideal GaN and AlN layers are used without inserting a charge layer in between. Similarities between this plot and the plot of Figure 5.16 where a GaAs/AlGaAs system is used is very much apparent since a GaAs/AlGaAs system is much less polarization induced charges due to the structure's smaller lattice mismatch.

In the following a series of I-V simulations are presented in Figures 5.26, 5.27, 5.28, 5.29, 5.30, 5.31 and 5.32. The results of these I-V simulations are not very satisfactory since the simulator didn't deliver continuous graphs as it would be expected in a real measurement. Still some conclusions could be made.

a-plane DBRTD simulations suggest:

- General conclusions from the polar simulations still apply.

- A shift of the I-V curve to the right could be observed in all graphs. This is a general advantage if biased operation is required in a circuit.

- Single band current estimation is poor, being several orders of magnitude less than the results in the polar structures.

5.5 Experimental Results

5.5.1 Growth

Wafers HFTS-189, HFTS-191 and HFTS-232 were grown on c-plane sapphire (c-plane GaN). Their construction is shown in Table 5.1.

Table 5.1 shows a summary of the grown substrates for the RTDs. The cladding layer of HFTS-191 was divided into two parts of 125nm and then 25nm on the top, with $8 \times 10^{17} cm^{-3}$ and $8.32 \times 10^{18} cm^{-3}$ respectively to study the effect of gradual doping in the quality of the surface morphology.

5.6 Measurements

Diodes were fabricated in the same manner as the single barrier diodes. Specially for the case of double barrier diodes, a new mask was created to allow experiments with smaller sized diodes down to $4\mu m$. This mask is depicted in figure B.3 and was not used in the course of this work due to lack of time.

5.6.1 c-Plane RTD Measurements

The I-V characteristics of the c-plane RTD grown on HFTS-189 wafer could be seen in Figure 5.34 where the first trace is labeled as M1 and the retrace of the measurement is labeled as M2. The measured diode had a diameter of $16\mu m$. It could be seen that

Wafer Name	Structure	Cap Doping	Results
HFTS-189	GaN 30 nm / AlN ~6 nm / GaN ~5 nm / AlN ~6 nm / GaN 30 nm	Top : $4.2 \times 10^{18} cm^{-3}$ $Bottom$: $3.0 \times 10^{18} cm^{-3}$	Diode measurements done
HFTS-191	Same as HFTS-189	Same as HFTS-189 but top cladding with 125nm of $8 \times 10^{17} cm^{-3}$ and 25nm of $8.32 \times 10^{18} cm^{-3}$	Poor quality, no devices worked
HFTS-232	GaN 30 nm / AlN ~6 nm / GaN ~4 nm / AlN ~6 nm / GaN 30 nm	Same as HFTS-189	Results still in Progress

Table 5.1: Wafers grown for c-plane double barrier RTDs

by successive measurements the peak of the amplitude is reduced. A zoomed-out version of the same measurement curve could be seen in Figure 5.35

The measured PVCR was about 1.3 at a voltage of 2.1V and a current density of $3326 Acm^{-2}$. The resulting I-V curve has an abrupt form which is different from the I-V curves of other conventional material systems such as GaAs/AlGaAs.

Other samples either had a poor fabrication quality, which caused a short or open behavior, or showed resistive characteristics. Another set of diodes had the exponential background as if the double barrier were physically merged like a single barrier diode.

5.7 Discussion

From the theoretical discussions, it could be concluded that symmetric barriers are needed for good resonance conditions. They cause sharp peaks in the transmission probability.

The measurement results of HFTS-189 showed some indications of NDR effect with a PVCR of about 1.3 at a current density of $3326Acm^{-2}$. The results have still don't posses adequate quality and should be seen as a preliminary of better works in future. Nevertheless these observations seem to have much in common with the observations of other groups in the recently published papers.

- Most of the diodes show only the exponential background, i.e. mostly both barriers behave like a single barrier. This was confirmed by Golka et. al. [42] and Leconte et. al. [43]. This might be due to existence of a large number of dislocations in the well.

- The sample HFTS-189-D3 showed very abrupt NDR which was also confirmed by [37], [38], [40], [41], [42] and [43]. The results in [42] show the existence of a third type with "smooth" NDR, which the author couldn't observe in the measurements.

- The NDR has a peak to valley ratio of roughly (1.3)

- The NDR takes place around a bias voltage of 2 Volts on the sample HFTS-189-D3 which was also experimentally confirmed by other papers as listed in Table 5.2).

- The reduction of current peak observed in this work can be due to charge trapping. This is also confirmed by [42] and [43]. A thermal treatment recovers these devices as described in [42].

- Voltage at which discontinuities occur are random as was the case for [42].

- Most researchers are conservative about using the term "NDR" for these current behaviors, due to current instabilities and lack of reproducibility.

- Most of these instabilities are caused by traps, dislocation densities and micro-cracks due to e.g. accumulation of strain of the AlN layer and passing it to the cap layer [43].

Table 5.2 shows a summary of the RTD works and the results of the present work. It could be seen that best results (smoothest NDR curves) have been achieved by dislocation densities of about $10^2 cm^{-2}$.

Author/Reference	Date	Method	Disl. Dens.	I_{peak}	@V_{res}	PVCR	Cap Doping	Mesa ⌀
Kikuchi et. al. [37]	2002	MBE	N/A	$180 Acm^{-2}$	2.4V	32	$N_S = 8 \times 10^{18} cm^{-3}$	$40\mu m$
Kishino et. al. [40]	2002	MBE	$3 \times 10^{8} cm^{-2}$	$930 mAcm^{-2}$	2.4V	3.1	$N_S = 8 \times 10^{17} cm^{-3}$	N/A
Foxon et. al. [41]	2003	MBE	$2 \times 10^{9} cm^{-2}$	$-40\mu A$	-6V	4	N/A	$100\mu m$
Hermann et. al. [6]	2004	MBE	$2 \times 10^{9} cm^{-2}$	$600\mu Acm^{-2}$	1V	8.3	$N_S = 8 \times 10^{18} cm^{-3}$	N/A
Golka et. al. [42]	2006	MBE	$10^{2} cm^{-2}$	10mA	2.4	2	$N_S = 5 \times 10^{18} cm^{-3}$	$6\mu m$
Leconte et. al. [43]	2008	MBE	$5 \times 10^{8} cm^{-2}$	$45\mu A$	1.5	3.2	10^{19}	$6\mu m$
Present work	2009	MOCVD	N/A	$3326 Acm^{-2}$	2.1V	1.3	$N_S = 4.2 \times 10^{18} cm^{-3}$	$16\mu m$

Table 5.2: Summary of the existing results on c-plane III-nitride based DB-RTD and results of the present work

In order to remedy these problems one needs to grow high quality material on the one hand, and reduce the lateral size of the mesa on the other hand. This leads to a high possibility of having the working device on top of the dislocation free region.

The smallest mesa sizes used in this work were $12\mu m$ and $16\mu m$. No satisfactory results were observed from other diodes of larger sizes. Now the smaller the diodes, the harder it gets to make contacts for measurements on such small sizes of diodes. Good contacts could be made with gold whiskers, but these inturn need to be securely fixed on the devices. Electrical contact with tungsten needle in search of best electrical contact, already "spoils" the chance of first measurements before the charge trapping occurs.

A solution to the contact problem was designing a mask with large pad connections with a silicon nitride passivation layer in between. This mask was produced but not used during this work because of the limitations of time. This sort of fabrication process has already been used by Golka et. al. in [42] where mesa sizes down to $6\mu m$ were achieved.
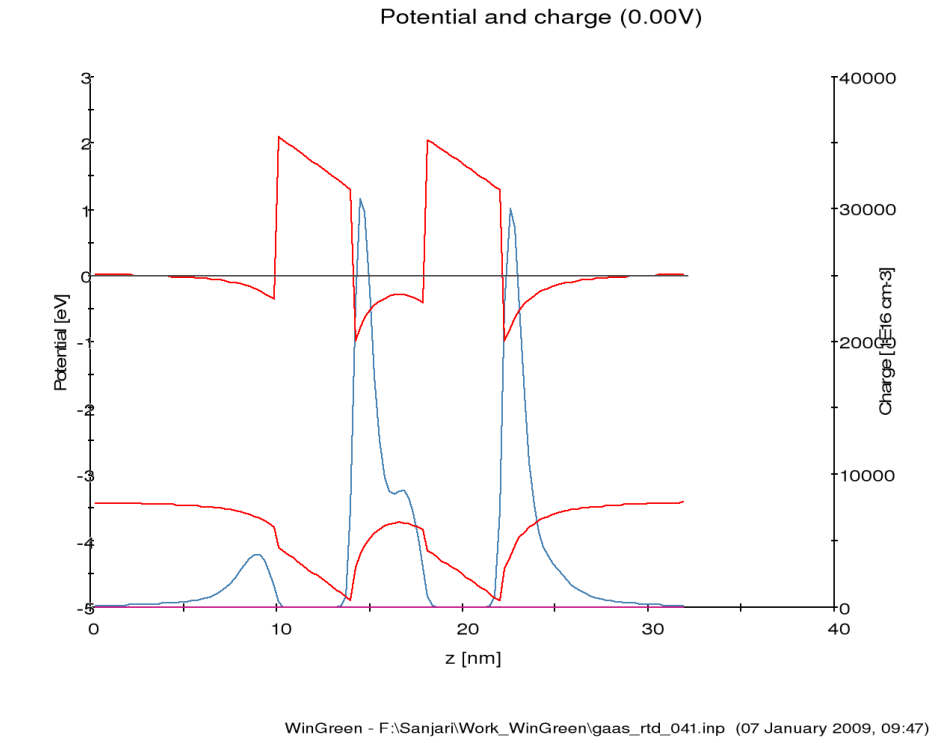
(a) $V_B = 0V$ (Charge accumulation is visible)
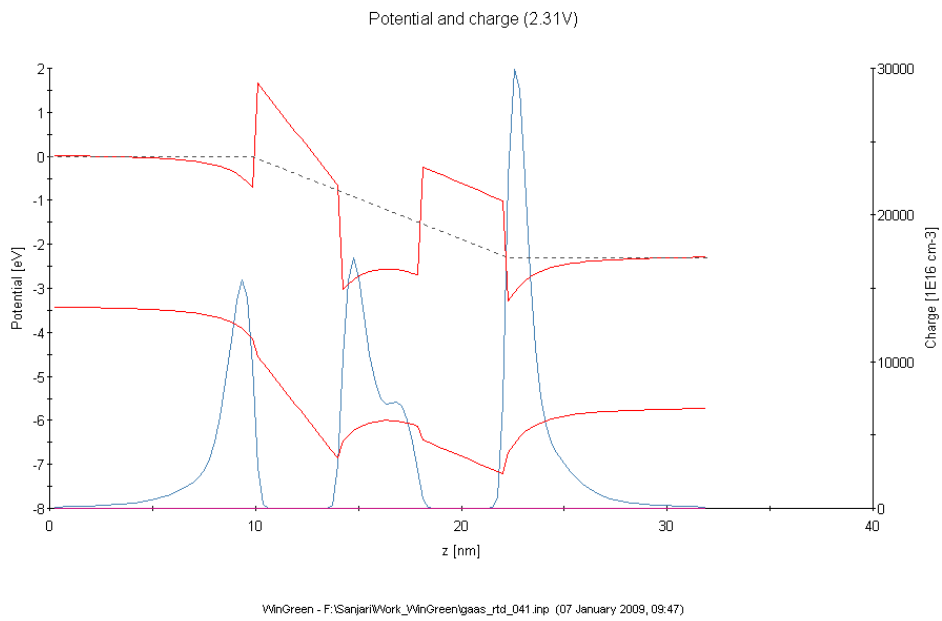
(b) $V_B = 2.31V$

Figure 5.14: Simulated potential and charge plots for a well and barrier thickness of 4nm

Local density of states (0.00V)

(a) $V_B = 0V$

Local density of states (2.31V)

(b) $V_B = 2.31V$
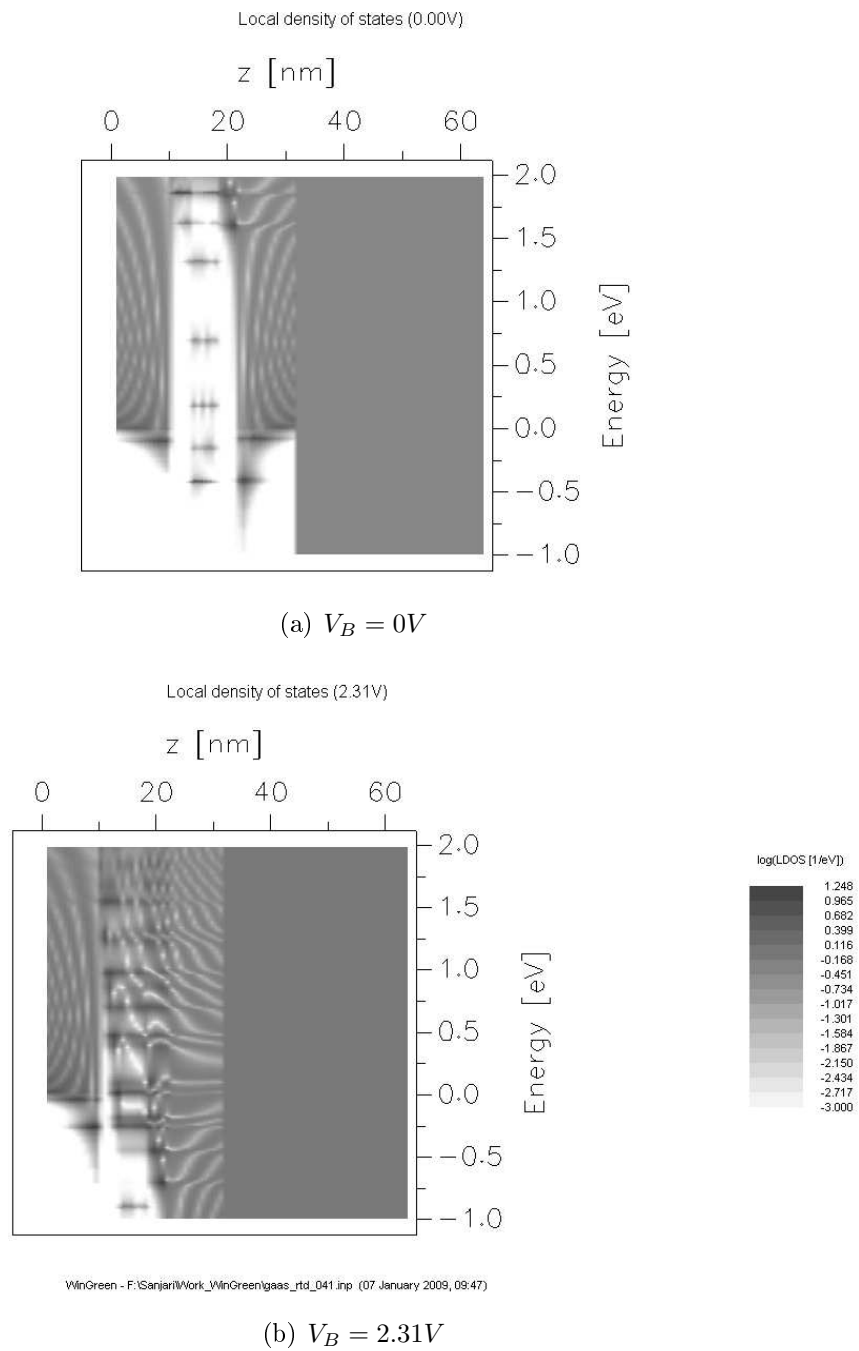
Figure 5.15: Simulated local density of states plots for a well and barrier thickness of 4nm (same structure as Figure 5.14

Potential and charge (0.00V)
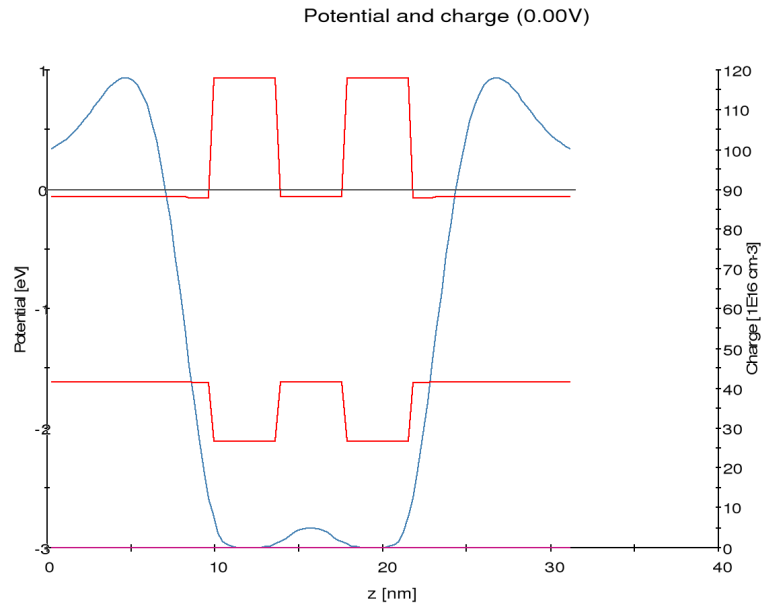
WinGreen - F:\Sanjari\Work_WinGreen\gaas_rtd_057_gaas.inp (19 January 2009, 09:43)

(a) $V_B = 0V$

Potential and charge (2.37V)
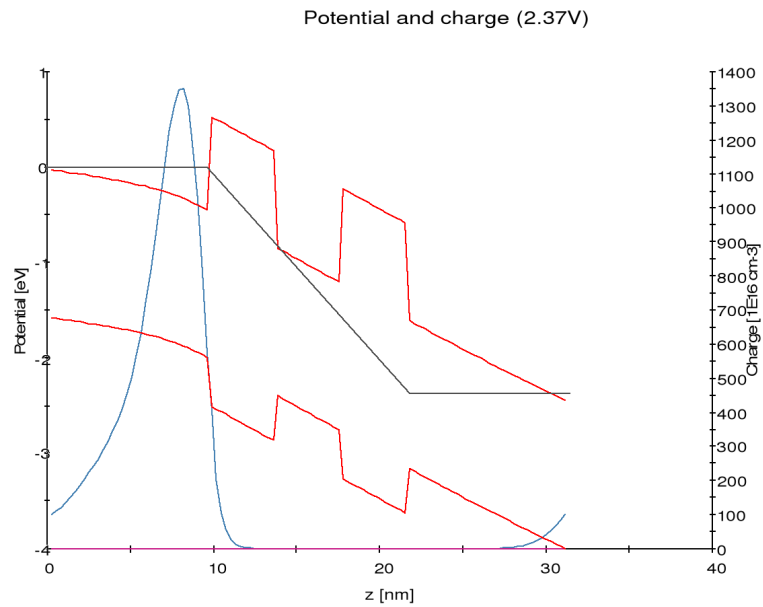
WinGreen - F:\Sanjari\Work_WinGreen\gaas_rtd_057_gaas.inp (19 January 2009, 09:43)

(b) $V_B = 2.37V$

Figure 5.16: Simulated potential and charge plots for a well and barrier thickness of 4nm using full band GaAs/AlGaAs model
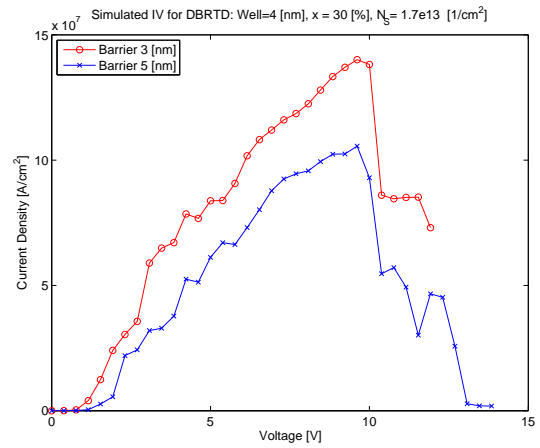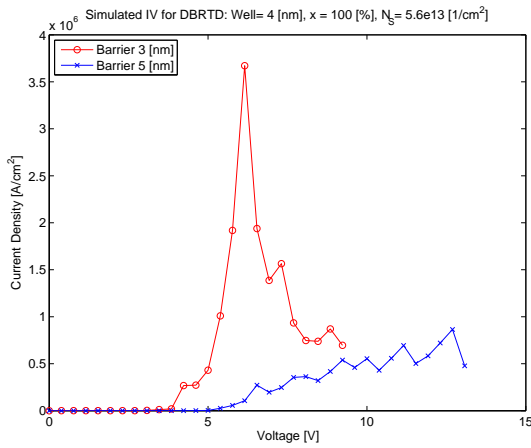
Figure 5.17: Well=4nm,x=100%,$\sigma = 5.6 \times 10^{13}cm^{-2}$

Figure 5.18: Well=4nm,x=30%,$\sigma = 1.7 \times 10^{13}cm^{-2}$
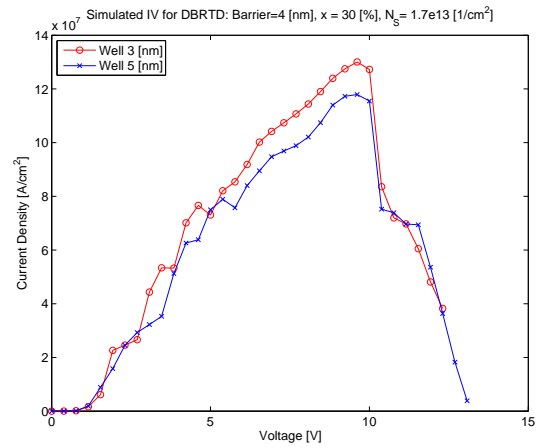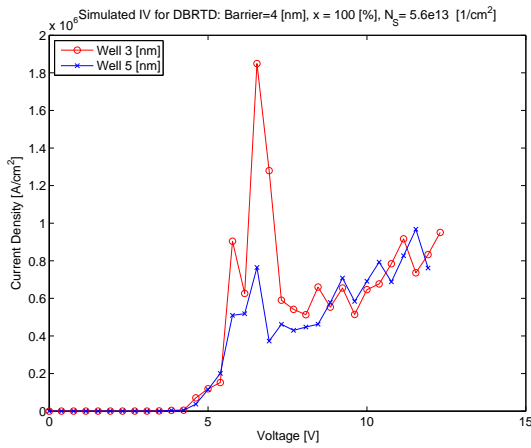
Figure 5.19: Barrier=4nm,x=100%,$\sigma = 5.6 \times 10^{13}cm^{-2}$

Figure 5.20: Barrier=4nm,x=30%,$\sigma = 1.7 \times 10^{13}cm^{-2}$
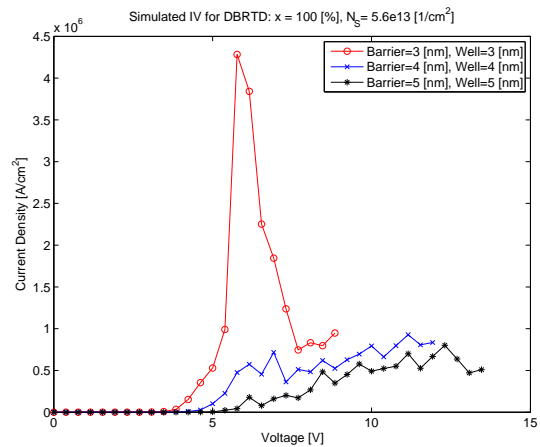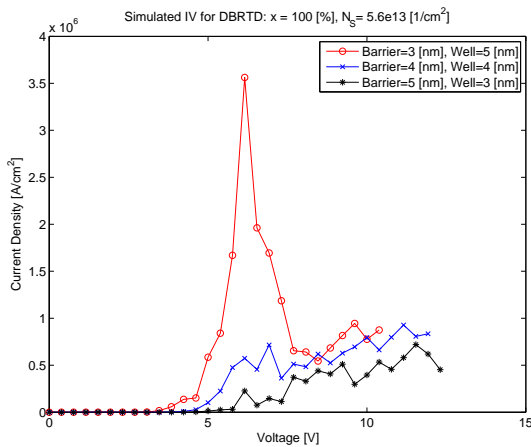
Figure 5.21: x=100%,$\sigma = 5.6 \times 10^{13}cm^{-2}$

Figure 5.22: x=100%,$\sigma = 5.6 \times 10^{13}cm^{-2}$
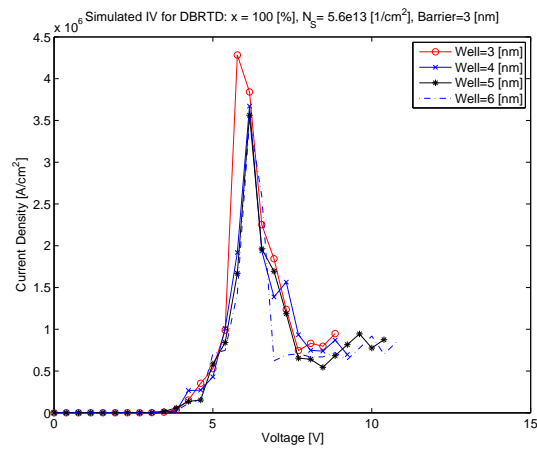
Figure 5.23: Barrier=3nm, x=100%, $\sigma = 5.6 \times 10^{13} cm^{-2}$
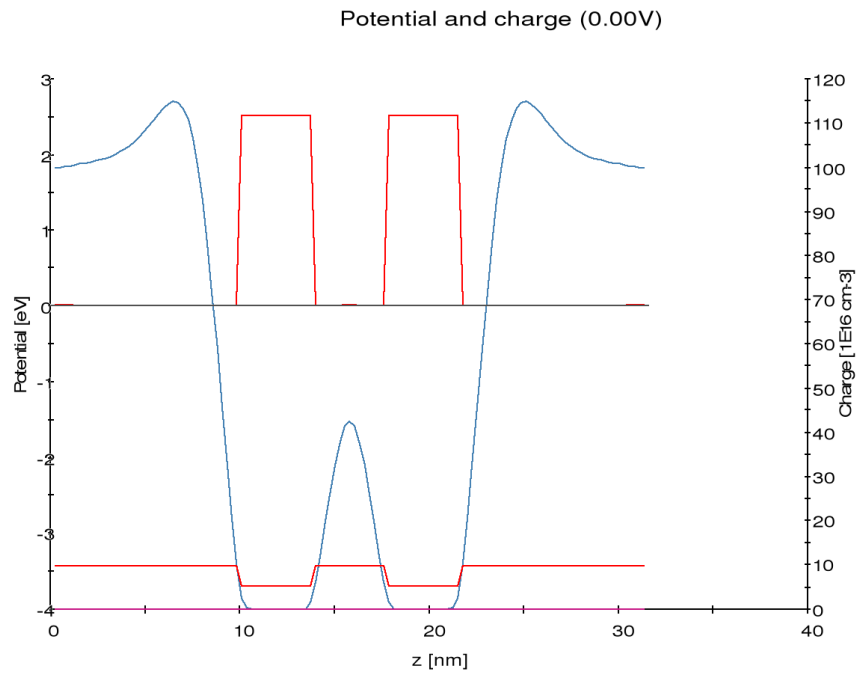
(a) $V_B = 0V$
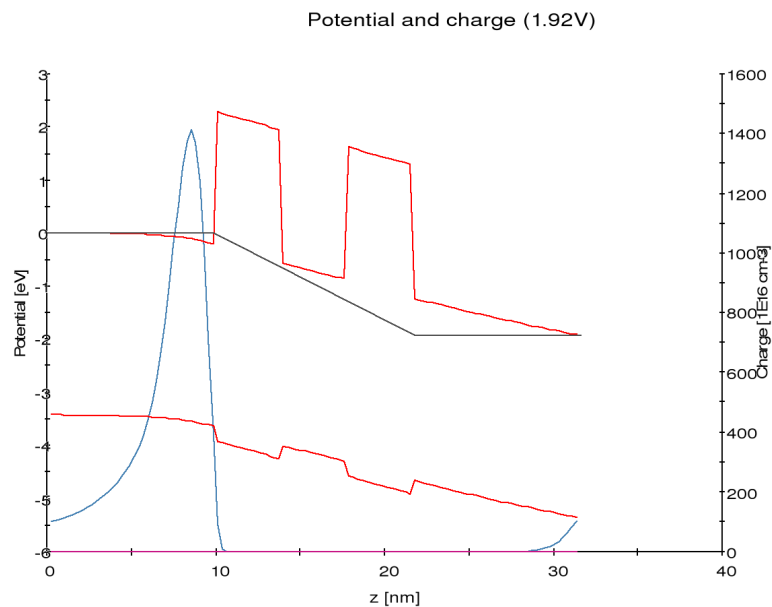
(b) $V_B = 1.92V$

Figure 5.24: Simulated potential and charge plots for a well and barrier thickness of 4nm for the non-polar structure (polarization charge is zero)

Local density of states (0.00V)

z [nm]
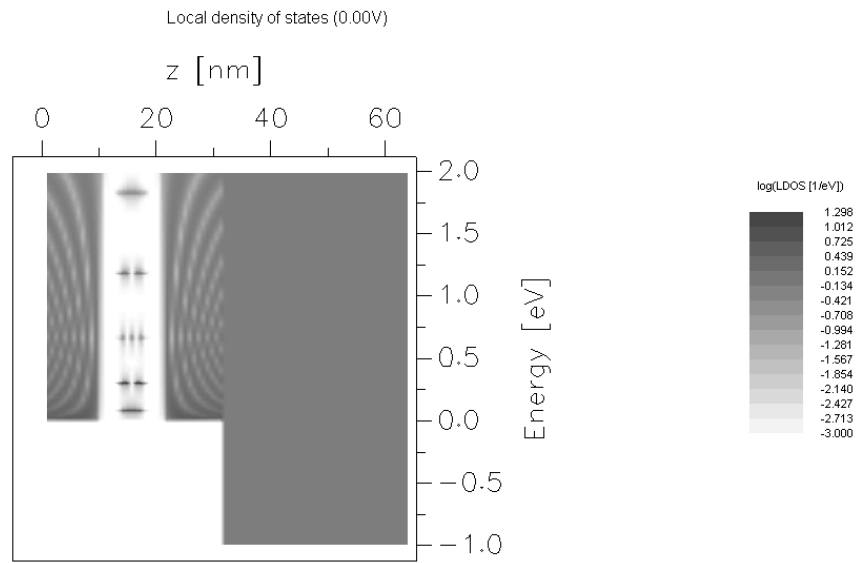
WinGreen - F:\Sanjari\Work_WinGreen\gaas_rtd_057.inp (07 January 2009, 09:47)

(a) $V_B = 0V$

Local density of states (1.92V)

z [nm]
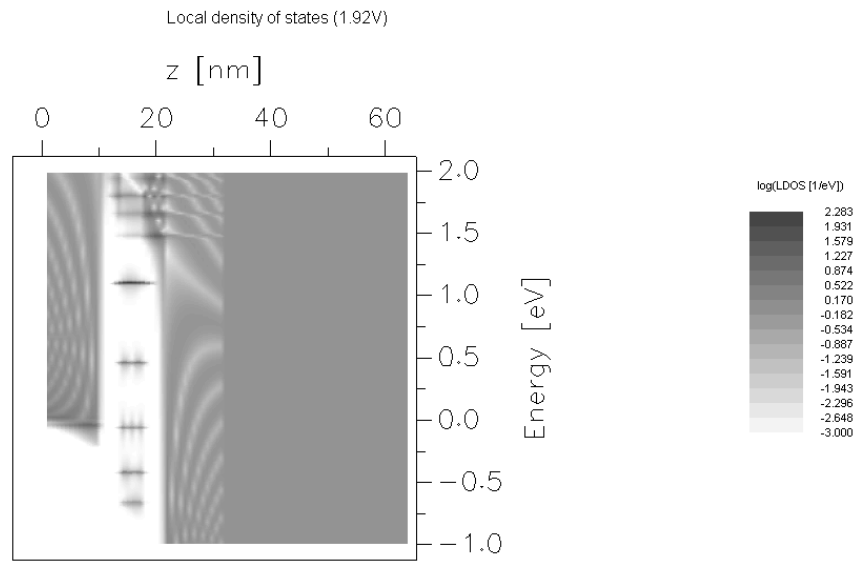
WinGreen - F:\Sanjari\Work_WinGreen\gaas_rtd_057.inp (07 January 2009, 09:47)

(b) $V_B = 1.92V$

Figure 5.25: Simulated local density of states plots for a well and barrier thickness of 4nm for the non polar structure
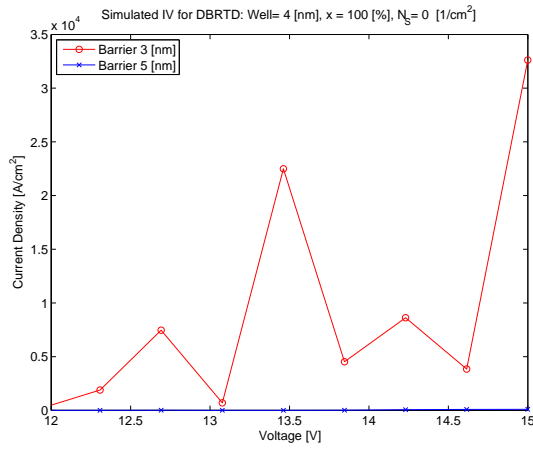
Figure 5.26: Well=4nm,x=100%
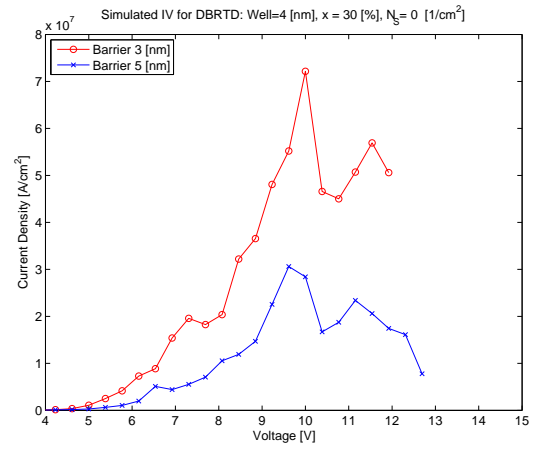
Figure 5.27: Well=4nm,x=30%
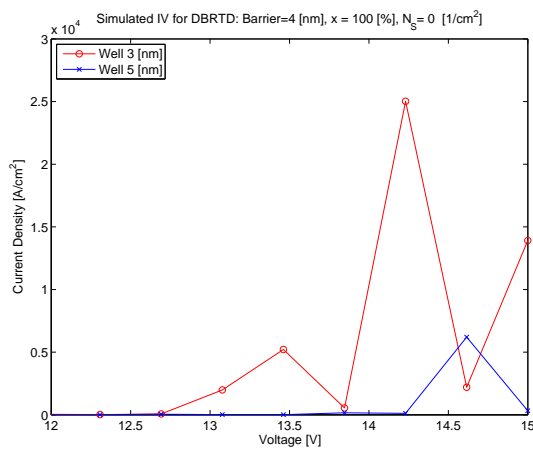
Figure 5.28: Barrier=4nm,x=100%
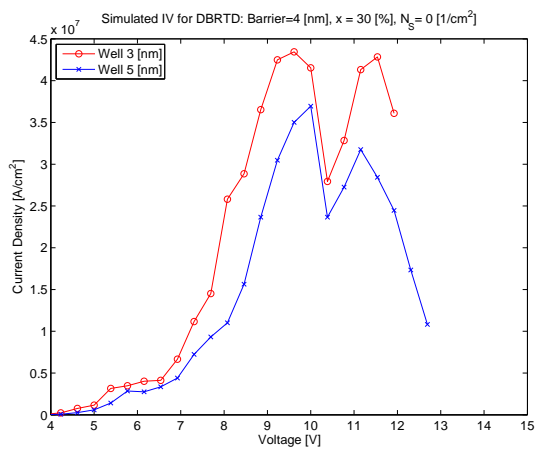
Figure 5.29: Barrier=4nm,x=30%
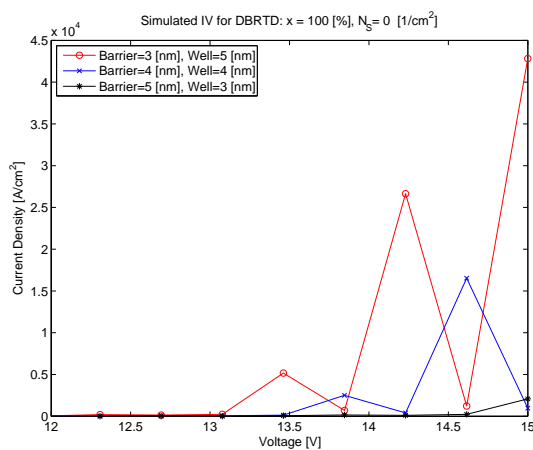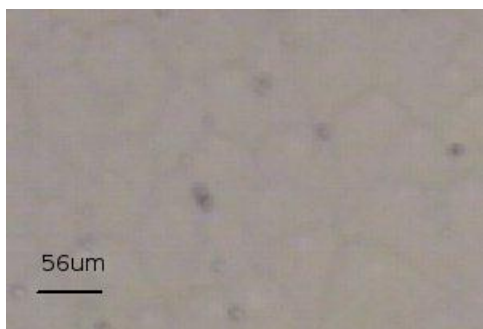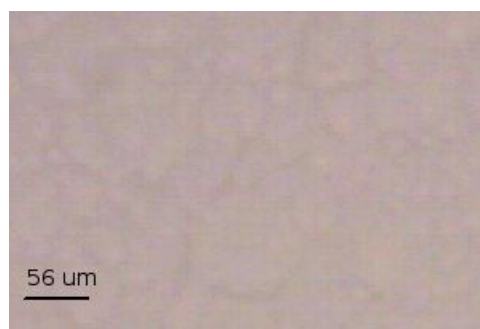

Figure 5.30: x=100%
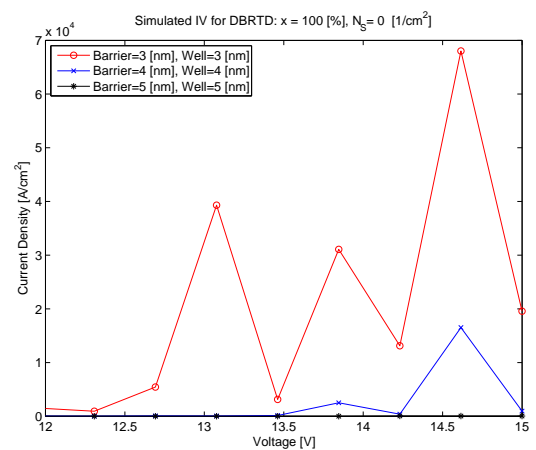
Figure 5.31: x=100%
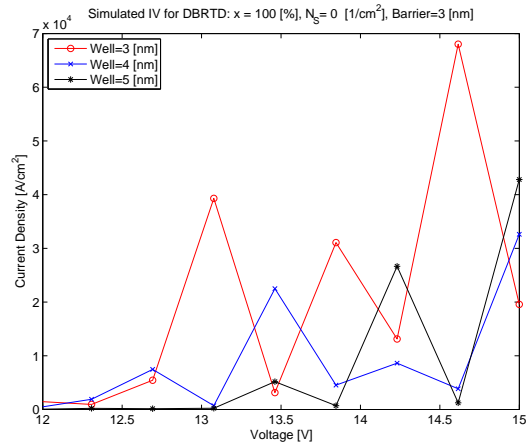
Figure 5.32: Barrier=3nm, x=100%

(a) Surface of HFTS-189   (b) Surface of HFTS-232

Figure 5.33: Surface morphology of the grown for DB-RTD wafers with a 5:1 magnification
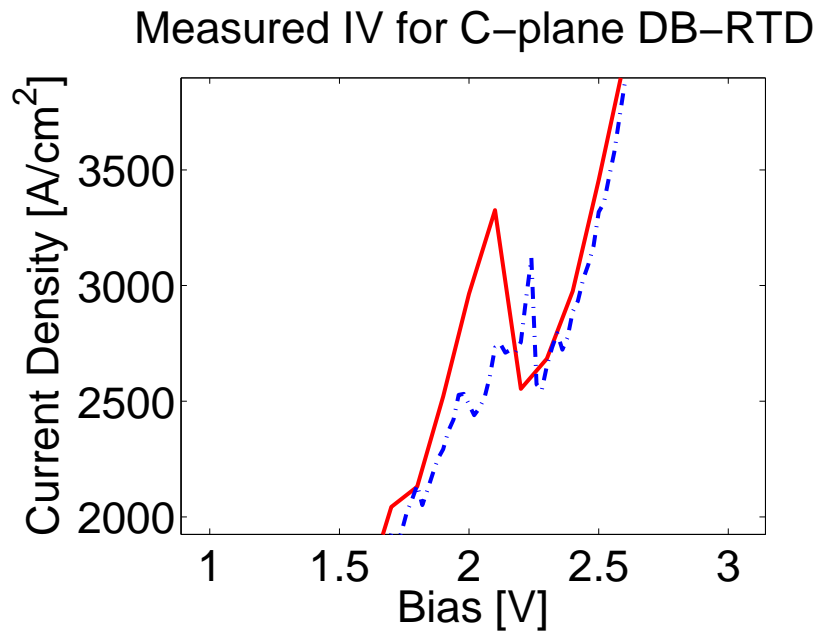
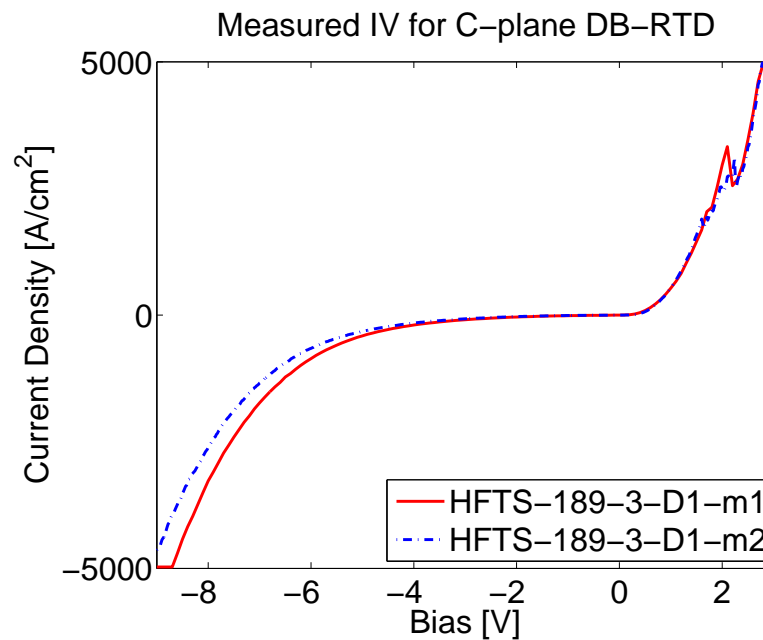Figure 5.34: Measured I-V characteristics of the HFTS-189 c-plane DB-RTD

Figure 5.35: Zoomed out: Measured I-V characteristics of the HFTS-189 c-plane DB-RTD

6 Summary and Outlook

In this work, resonant tunneling diodes based on polar and non-polar III-Nitride materials were investigated. The author tried to cover the most important steps towards physical realization of GaN-Based resonant Tunneling diodes. Quantum mechanical concepts were studied in order to understand different aspects of resonant tuneling.

- Realization of single barrier structures for the study of charge transport across the barrier.

- Realization of double barrier structures based on c-plane GaN.

- Review of some of the theoretical background needed to calculate GaN specific parameters

- Simulations based on 1-band model for realized GaN heterostructures

The work could be further detailed in the following ways:

- NextNano3 software package can be used for calculations using full band model. This can provide better I-V curve predictions and peak current density estimations.

- Use the new DC mask which is depicted in Figure B.3 with reduced mesa sizes and Silicon oxide or Silicon nitride passivation and use Gold whiskers to form contacts.

- Investigate other growth methods (like e.g. flow rate modulation, where the metal organic flow is periodically interrupted) as in [45] to obtain higher quality material in well an barrier regions. A better quality in these layers would enable sharp interfaces which in turn result in better transmission characteristics.

- Investigate growth on top of free standing a-plane GaN substrates.

- Investigate effect of gradual doping in the cladding layers and see if the performance of RTDs could be improved. Gradual doping would eliminate sudden changes in the crystal structure due to the existence of impurities.

- Investigate how equation 3.22 would look like for a-plane GaN.

- Investigate how Polyimide could be used to make stable Gold whisker contacts as in [2].

- Investigate the benefits of pulsed I-V measurement.

- Grow samples with different well thicknesses, so that tunneling current could be confirmed.

Bibliography

[1] Leo Esaki. New phenomenon in narrow germanium p-n junction. *Phys. Rev.*, 109:603, 1958.

[2] Imran Mehdi. *Device Applications of double barrier resonant tunneling structures*. PhD thesis, The University of Michgan, 1990.

[3] N. Orihashi, S. Suzuki, and M. Asada. One THz harmonic oscillation of resonant tunneling diodes. *Applied Physics Letters*, 87:233501, 2005.

[4] S.F. Chichibu, A.C. Abare, MS Minsky, S. Keller, S.B. Fleischer, J.E. Bowers, E. Hu, U. Mishra, L.A. Coldren, S.P. DenBaars, et al. Effective band gap inhomogeneity and piezoelectric field in InGaN/GaN multiquantum well structures. *Applied Physics Letters*, 73:2006, 1998.

[5] CK Choi, YH Kwon, BD Little, G.H. Gainer, J.J. Song, Y.C. Chang, S. Keller, U. Mishra, and S.P. DenBaars. Time-resolved photoluminescence of In_ {x} Ga_ {1-x} N/GaN multiple quantum well structures: Effect of Si doping in the barriers. *Physical Review B*, 64(24):245339, 2001.

[6] M. Hermann, E. Monroy, A. Helman, B. Baur, M. Albrecht, B. Daudin, O. Ambacher, M. Stutzmann, and M. Eickhoff. Vertical transport in group III-nitride heterostructures and application in AlN/GaN resonant tunneling diodes. *PHYSICA STATUS SOLIDI C CONFERENCES*, 1(8):2210–2227, 2004.

[7] O. Ambacher, M. Eickhoff, A. Link, M. Hermann, M. Stutzmann, F. Bernardini, V. Fiorentini, Y. Smorchkova, J. Speck, U. Mishra, et al. Electronics and sensors based on pyroelectric A 1 GaN/GaN heterostructures; Part A: Polarization and pyroelectronics. In *Phys. Status Solidi- Conf.*, pages 1878–1907, 2003.

[8] Thomas Swan Scientific Equipment Ltd., Anderson Rd. Buckingway Buisiness Park, Swavesey, Cambridge, CB45FQ, UK. *Thomas Swan In-Situ Reflectance Monitor*, May 2002.

[9] NM NASSER, Y. Zhizhen, L. Jiawei, et al. GaN Heteroepitaxial Growth Techniques [J]. *Journal of Microwaves and Optoelectronics*, 2(3):22–31, 2001.

[10] H. Chung and C. Wang. Annual report. Technical report, Department of Optoelectronics, University of Ulm, Germany, 1999.

[11] J.H. Edgar, Knovel, and INSPEC. *Properties of Group III Nitrides.* INSPEC, the Institution of Electrical Engineers, 1994.

[12] O. Ambacher, J. Smart, J.R. Shealy, N.G. Weimann, K. Chu, M. Murphy, W.J. Schaff, L.F. Eastman, R. Dimitrov, L. Wittmer, et al. Two-dimensional electron gases induced by spontaneous and piezoelectric polarization charges in N-and Ga-face AlGaN/GaN heterostructures. *Journal of Applied Physics*, 85:3222, 1999.

[13] M. Kuroda, H. Ishida, T. Ueda, and T. Tanaka. Nonpolar (11-20) plane AlGaN/GaN heterojunction field effect transistors on (1-102) plane sapphire. *Journal of Applied Physics*, 102:093703, 2007.

[14] S. Ghosh, P. Misra, H.T. Grahn, B. Imer, S. Nakamura, S.P. DenBaars, and J. Speck. Polarized photoreflectance spectroscopy of strained A-plane GaN films on R-plane sapphire. *Journal of Applied Physics*, 98:026105, 2005.

[15] M.A. Khan, Q. Chen, C.J. Sun, J.W. Yang, M. Blasingame, M Shur, and H. Park. Enhancement and depletion mode GaN/AlGaN heterostructure field effect transistors. *Applied Physics Letters*, 68:514, 1996.

[16] V. Kumar, A. Kuliev, T. Tanaka, Y. Otoki, and I. Adesida. High transconductance enhancement-mode AlGaN/GaN HEMTs on SiC substrate. *Electronics Letters*, 39(24):1758–1760, 2003.

[17] V. Palankovski and R. Quay. *Analysis and Simulation of Heterostructure Devices.* Springer, 2004.

[18] P. Harrison, J. Wiley, and W. InterScience. *Quantum Wells, Wires and Dots: Theoretical and Computational Physics of Semiconductor Nanostructures.* Wiley, 2005.

[19] Eoin P. O'Reilly. *Quantum Theory of Solids.* Masters Series in Physics and Astronomy. Taylor & Francis, first edition, 2002.

[20] W. Trzeciakowski. Effective-mass approximation in semiconductor heterostructures: One-dimensional analysis. *Physical Review B*, 38(17):12493–12507, 1988.

[21] Gerhard Klimeck, R. Lake, R.C. Bowen, W.R. Frensley, and T.S. Moise. Quantum device simulation with a generalized tunneling formula. *Applied Physics Letters*, 67:2539, 1995.

[22] D.Z.Y. Ting, ET Yu, and TC McGill. Multiband treatment of quantum transport in interband tunnel devices. *Physical Review B*, 45(7):3583–3592, 1992.

[23] T.B. Boykin, J.P.A. van der Wagt, and J.S. Harris Jr. Tight-binding model for GaAs/AlAs resonant-tunneling diodes. *Physical Review B*, 43(6):4777–4784, 1991.

[24] R.C. Bowen, Gerhard Klimeck, R. Lake, W.R. Frensley, and T. Moise. Quantitative simulation of a resonant tunneling diode. *Journal of Applied Physics*, 81:3207, 1997.

[25] Gerhard Klimeck. Bandstructure in nanoelectronics, Nov 2005.

[26] Walter A. Harrison. Bond-orbital model and the properties of tetrahedrally coordinated solids. *Phys. Rev. B*, 8(10):4487–4498, Nov 1973.

[27] P. Vogl, H.P. Hjalmarson, and J.D. Dow. Semi-empirical tight-binding theory of the electronic structure of semiconductors. *J. PHYS. CHEM. SOL.*, 44(5):265–378, 1983.

[28] D.K. Ferry. *Quantum Mechanics: An Introduction for Device Physicists and Electrical Engineers*. Inst of Physics Pub Inc, 2001.

[29] A. Bykhovski, B. Gelmont, and M. Shur. The influence of the strain-induced electric field on the charge distribution in GaN-AlN-GaN structure. *Journal of Applied Physics*, 74:6734, 1993.

[30] S. Leconte, F. Guillot, E. Sarigiannidou, and E. Monroy. Charge distribution and vertical electron transport through GaN/AlN/GaN single-barrier structures. *SEMICONDUCTOR SCIENCE AND TECHNOLOGY*, 22(2):107, 2007.

[31] K. M. Indlekofer and J. Malindretos. Wingreen simulation package.

[32] S. Datta and S. Yatta. *Quantum phenomena*. Addison-Wesley Reading, Mass, 1989.

[33] Anna Sigurdardóttir. *New Concepts for Submilimetre-Wave Power Generation Using Resonant-Tunneling Diodes*. PhD thesis, Darmstadt University of Technology, April 1999.

[34] WCB Peatman, E.R. Brown, MJ Rooks, P. Maki, W.J. Grimm, and M. Shur. Novel resonant tunneling transistor with high transconductance atroom temperature. *Electron Device Letters, IEEE*, 15(7):236–238, 1994.

[35] N. Yokoyama, K. Imamura, S. Muto, S. Hiyamizu, and H. Nishi. A new functional, resonant-tunneling hot electron transistor (RHET). *Jpn. J. Appl. Phys*, 24:L853–L854, 1985.

[36] P. Mazumder, S. Kulkarni, M. Bhattacharya, J.P. Sun, and G.I. Haddad. Digital Circuit Applications of Resonant Tunneling Devices. *PROCEEDINGS OF THE IEEE*, 86(4), 1998.

[37] A. Kikuchi, R. Bannai, K. Kishino, C.M. Lee, and J.I. Chyi. AlN/GaN double-barrier resonant tunneling diodes grown by rf-plasma-assisted molecular-beam epitaxy. *Applied Physics Letters*, 81:1729, 2002.

[38] A. Kikuchi, R. Bannai, K. Kishino, C.M. Lee, and J.I. Chyi. Response to "Comment on 'AlN/GaN double-barrier resonant tunneling diodes grown by rf-plasma-assisted molecular-beam epitaxy'"[Appl. Phys. Lett.[bold 83], 3626 (2003)]. *Applied Physics Letters*, 83:3628, 2003.

[39] A.E. Belyaev, C.T. Foxon, SV Novikov, O. Makarovsky, L. Eaves, M.J. Kappers, and C.J. Humphreys. Comment on "AlN/GaN double-barrier resonant tunneling diodes grown by rf-plasma-assisted molecular-beam epitaxy"[Appl. Phys. Lett.[bold 81], 1729 (2002)]. *Applied Physics Letters*, 83:3626, 2003.

[40] K. Kishino and A. Kikuchi. Improved Molecular Beam Epitaxy for Fabricating AlGaN/GaN Heterojunction Devices. *physica status solidi(a)*, 190(1):23–31, 2002.

[41] CT Foxon, SV Novikov, AE Belyaev, LX Zhao, O. Makarovsky, DJ Walker, L. Eaves, RI Dykeman, SV Danylyuk, SA Vitusevich, et al. Current–voltage instabilities in GaN/AlGaN resonant Tunneling structures. *physica status solidi(c)*, pages 2389–2392, 2003.

[42] S. Golka, C. Pflügl, W. Schrenk, Gottfried Strasser, C. Skierbiszewski, M. Siekacz, I. Grzegory, and S. Porowski. Negative differential resistance in dislocation-free GaN/ AlGaN double-barrier diodes grown on bulk GaN. *Applied Physics Letters*, 88:172106, 2006.

[43] S. Leconte, S. Golka, G. Pozzovivo, Gottfried Strasser, T. Remmele, M. Albrecht, and E. Monroy. Bi-stable behaviour in GaN-based resonant Tunneling diode structures. *PHYSICA STATUS SOLIDI C CONFERENCES*, 5(2):431, 2008.

[44] Michael McLennan. Resonant tunneling diode simulator, Oct 2005.

[45] J.J. Huang, T.Y. Tang, C.F. Huang, and C.C. Yang. High-quality a-plane GaN grown with flow-rate modulation epitaxy on r-plane sapphire substrate. *Journal of Crystal Growth*, 310(11):2712–2716, 2008.

[46] Sanghyun Seo. AlGaNGaN High Electron Mobility Transistors *HEMTs*.

[47] Th. G. van de Roer. Modeling of double barrier resonant tunnelling diodes: D.c. and noise model. Eindhoven University of Technology.

[48] Christian Koch and J. Rinke. Lithography: Theory and application of photoresists, developers, solvents and echants. MicroChemicals GmbH, Schillerstrasse 18, D-89077 Ulm, 2007.

[49] Uli Kazmaier Helmut A. Klein Hans P. Latscha. *Organische Chemie*. Springer, Berlin, 6 edition, 2008.

[50] Yield Engineering Systems Inc. Descumming. http://www.yieldengineering.com/default.asp?page=245[15-08-05], 2008.

[51] E. Monroy, N. Gogneau, and E. Sarigiannidou. Comparison of the structural quality in ga-face and n-face polarity ganaln multiple-quantum-well structures. *Semiconductor Sci. Tech.*, pages 612–618, 2008.

[52] T.C. Wang, R.C. Gao, and T.S. Ko. Study on optimal growth conditions of a-plane gan grown on r-plane sapphire by metal-organic chemical vapor deposition. *Journal of Crystal Growth*, 300:308–313, 2007.

[53] H.F. Hameka. *Quantum Mechanics: A Conceptual Approach*. Wiley-Interscience, 2004.

[54] R.F. Pierret. *Semiconductor device fundamentals*. Addison-Wesley.

[55] S.M. Sze. *Physics of semiconductor devices*. 1981.

[56] S.M. Sze. *High-speed semiconductor devices*. 1990.

[57] S.M. Sze. *Semiconductor devices, physics and technology*. Wiley New York, 1985.

[58] S.M. Sze and I. NetLibrary. *Modern semiconductor device physics*. Wiley New York, 1998.

[59] S. Nakamura, Y. Harada, and M. Seno. Novel metalorganic chemical vapor deposition system for GaN growth. *Applied Physics Letters*, 58:2021, 1991.

[60] D.E. Aspnes. Real-time optical diagnostics for epitaxial growth. *Surface Science*, 307:1017–1027, 1994.

[61] A. Stafford, S.J.C. Irvine, K.L. Hess, and J. Bajaj. The use of in situ laser interferometry for MOCVD process control. *SEMICONDUCTOR SCIENCE AND TECHNOLOGY*, 13(12):1407–1411, 1998.

[62] Bragg's law. http://hyperphysics.phy-astr.gsu.edu/hbase/quantum/bragg.htm, 2008.

[63] X. Ni, Y. Fu, YT Moon, N. Biyikli, and H. Morkoç. Optimization of (112¯ 0) a-plane GaN growth by MOCVD on (11¯ 02) r-plane sapphire. *Journal of Crystal Growth*, 290(1):166–170, 2006.

[64] A. Reale, G. Massari, A. Di Carlo, P. Lugli, A. Vinattieri, D. Alderighi, M. Colocci, F. Semond, N. Grandjean, and J. Massies. Comprehensive description of the dynamical screening of the internal electric fields of AlGaN/GaN quantum wells in time-resolved photoluminescence experiments. *Journal of Applied Physics*, 93:400, 2002.

[65] C. Mailhiot, Y.C. Chang, and TC McGill. Energy spectra of donors in $GaAs/Ga_{1-x}Al_x$ As quantum well structures in the effective-mass approximation. *Physical Review B*, 26(8):4449–4457, 1982.

[66] L.I. Schiff. *Quantum mechanics*. Tokyo, 1968.

[67] Toshiyuki Nakamura, Hideaki Matsuhashi, and Yoshiki Nagatomo. Silicon on sapphire (sos) device technology. *OKi Technicak Review*, 71(4), October 2004.

[68] G. Gonzalez. *Microwave Transistor Amplifiers: Analysis and Design*. Prentice Hall New Jersey, 1997.

[69] *III-nitride resonant tunneling diodes*, Monte Verità, Swizerland, 2006. Summerschool on Wide-bandgap Semiconductor Quantum Structures.

A Used Abbreviations

2DEG	**2-D**imensional **E**lectron **G**as
AFM	**A**tomic **F**orce **M**icroscopy
DI Water	**D**e-**I**onised Water
C-AFM	**C**onductive **A**tomic **F**orce **M**icroscopy
EBE	**E**lectron **B**eam **E**vaporation
ELOG	**E**pitaxial **L**ateral **O**vergrowth
ERDA	**E**lastic **R**ecoil **D**etection **A**nalysis
FWHM	**F**ull **W**idth at **H**alf **M**aximum
HEMT	**H**igh **E**lectron **M**obility **T**ransistor
HMDS	**H**exa**m**ethyl-disilazane
IMPATT	**Imp**act **A**valanche **T**ransit **T**ime
IPA	**I**so-**P**ropyl **A**lcohol
LED	**L**ight **E**mitting **D**iode
MBE	**M**olecular **B**eam **E**pitaxy
MFC	**M**ass **F**low **C**ontroller
ML	**M**ono**l**ayer
MESFET	**Me**tal **S**emiconductor **F**ield **E**ffect **T**ransistor
MISFET	**M**etal **I**nsulator **S**emiconductor **F**ield **E**ffect **T**ransistor
MMIC	**M**icrowave **M**onolithic **I**ntegrated **C**ircuit
MOCVD	**M**etal **O**rganic **C**hemical **V**apor **D**eposition
MOVPE	**M**etal-**O**rganic Chemical **V**apour **P**hase **E**pitaxy
MQW	**M**ultiple **Q**uantum **W**ell
NDR	**N**egative **D**ifferential **R**esistance
NEGF	**N**on **E**quilibrium **G**reen's **F**unction
NFE	**N**early **F**ree **E**lectron
PAMBE	**P**lasma **A**ssisted **M**olecular **B**eam **E**pitaxy
PVCR	**P**eak to **V**alley **C**urrent **R**atio
QW	**Q**uantum **W**ell
RBS	**R**utherford **B**ackscattering **S**pectroscopy
RHET	**R**esonant tunneling **H**ot **E**lectron **T**ransistor
RIE	**R**eactive **I**on **E**tching
RMS	**R**oot **M**ean **S**quare
RPM	**R**ounds **P**er **M**inutes
RS-232	**R**ecommended **S**tandard 232

RTA	**R**apid **T**hermal **A**nnealing
RTD	**R**esonant **T**unneling **D**iode
sccm	**S**tandard **C**ubic **C**enti **M**eter
SIS	**S**emiconductor **I**nsulator **S**emiconductor
slm	**S**tandard **l**iter per **m**inute
SOI	**S**ilicon **o**n **I**nsulator
SOS	**S**ilicon **o**n **S**apphire
STP	**S**tandard **T**emperature and **P**ressure
TB	**T**ight **B**inding
TLM	**T**ransmission **L**ine **M**ethod
U.I.D.	**U**n**i**ntentionally **d**oped
UV	**U**ltra **V**iolet
VCA	**V**irtual **C**rystal **A**pproximation
VNA	**V**ector **N**etwork **A**nalyser
XRD	**x**-ray **D**iffraction

B Photolithography Mask Printouts

Some masks used during this work existed from previous research activities in the group. Some new masks were also designed by the author. Table B.1 lists the information about these masks.

Mask Name	Revision	Comments	Results
Diode with Airbridge Figure B.2	1998	Few number of circular diode patterns	was used and worked
HFE Diode Figure B.4	SEP08 by C. Jin	Anode pads were large	was used and worked
HFRTD01	SEP08 by M.S. Sanjari	Insufficient alignment marks	was not used
HFRTD02 Figure B.1	NOV08 by M.S. Sanjari	Sizes only down to $16\mu m$	was used and worked
DCRTD01 Figure B.3	DEC08 by M.S. Sanjari	Sizes down to $4\mu m$	for future use

Table B.1: Used Masks during this work.

Figure B.1: HFRTD Mask Version 2 by the Author
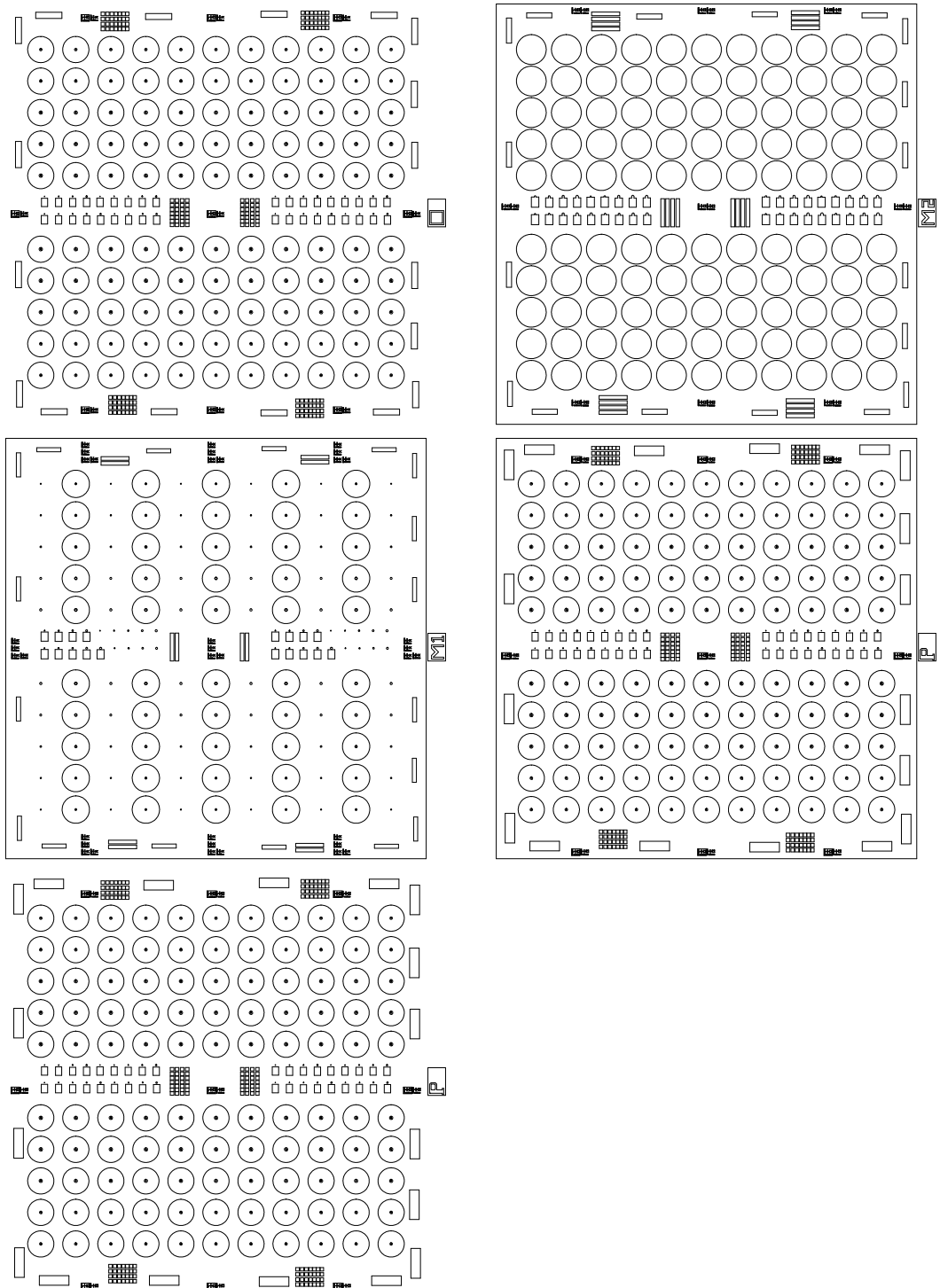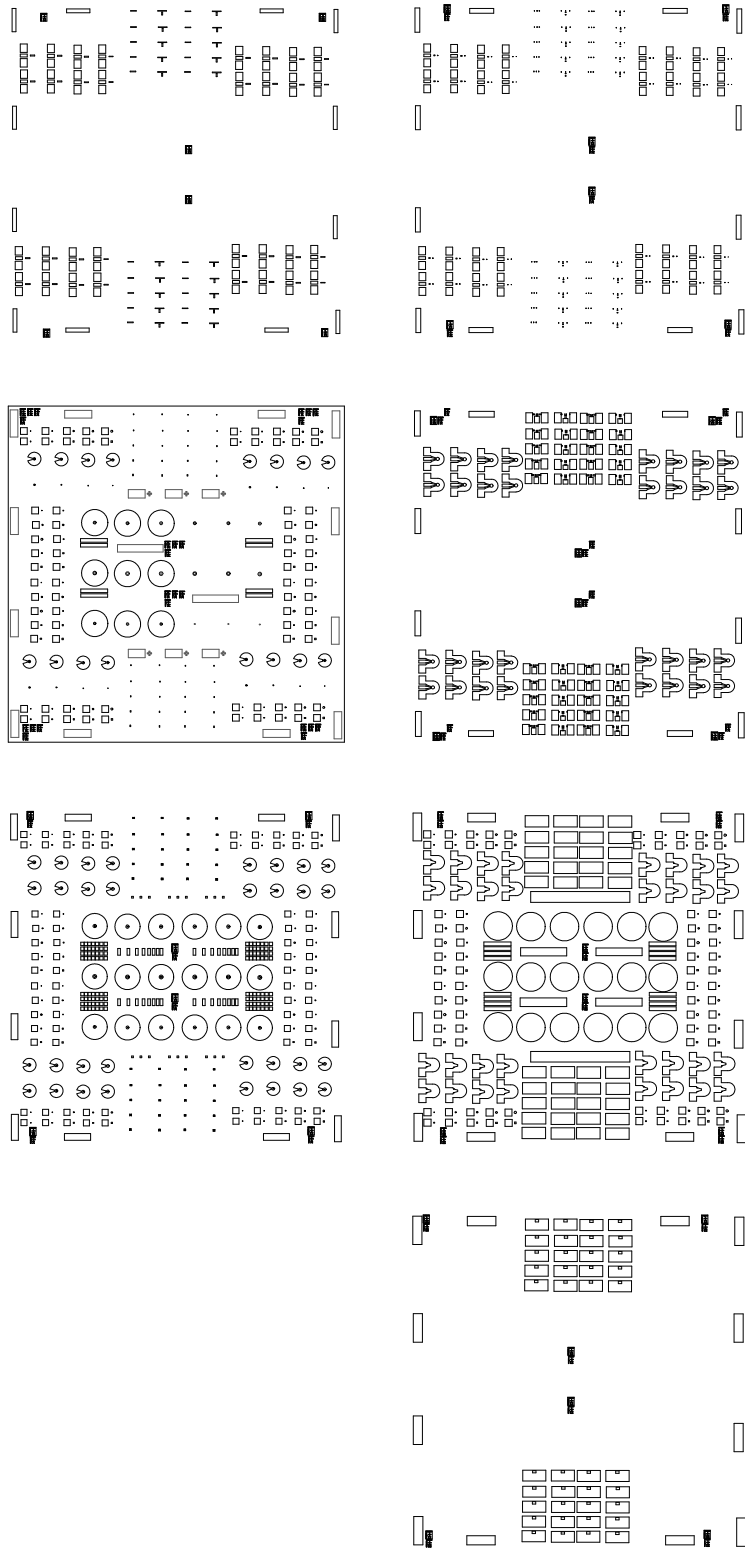
Figure B.2: Diode with Airbirdge (old, unknown Author)   97
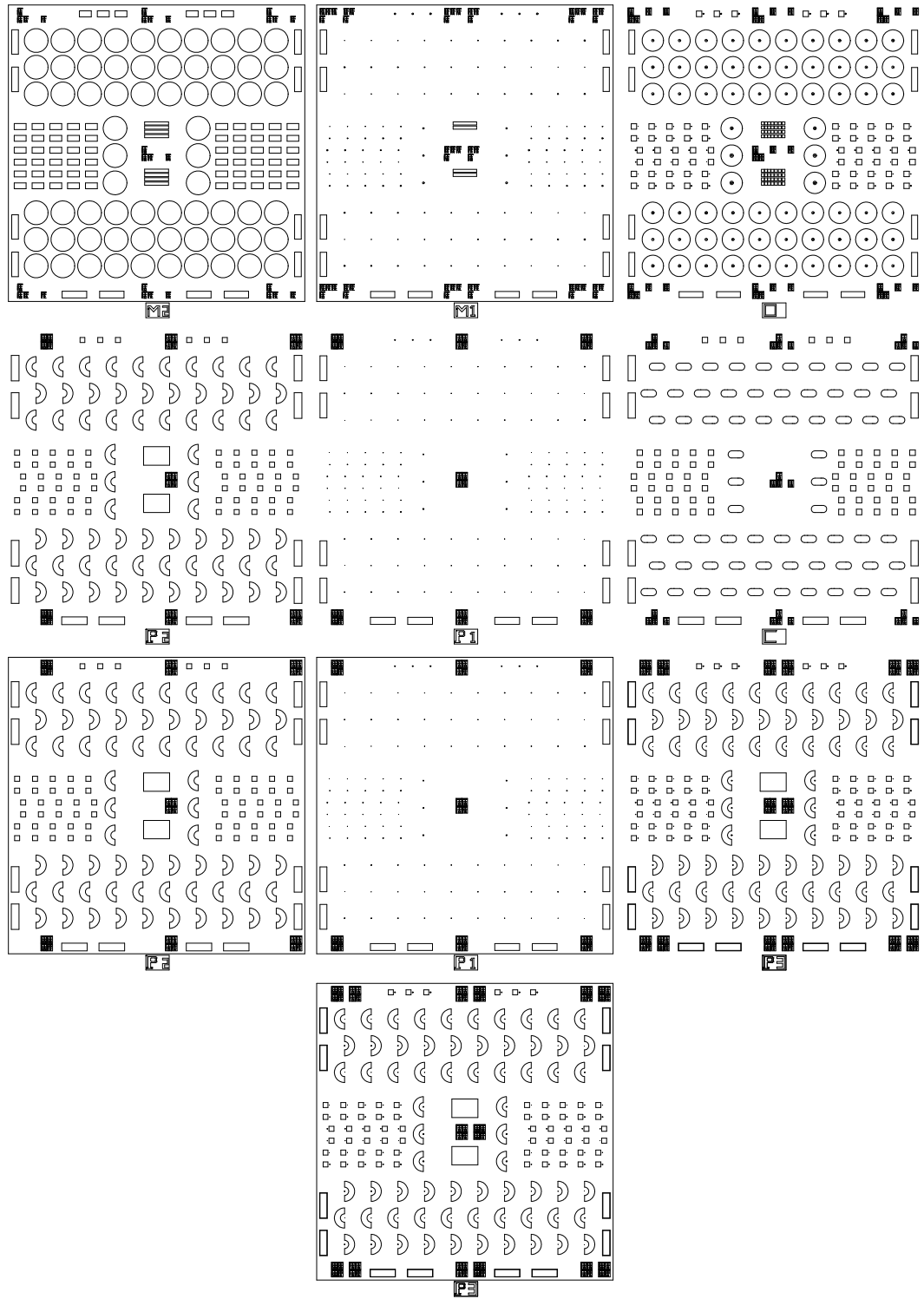
Figure B.3: DC-RTD Mask Version 1 by the Author
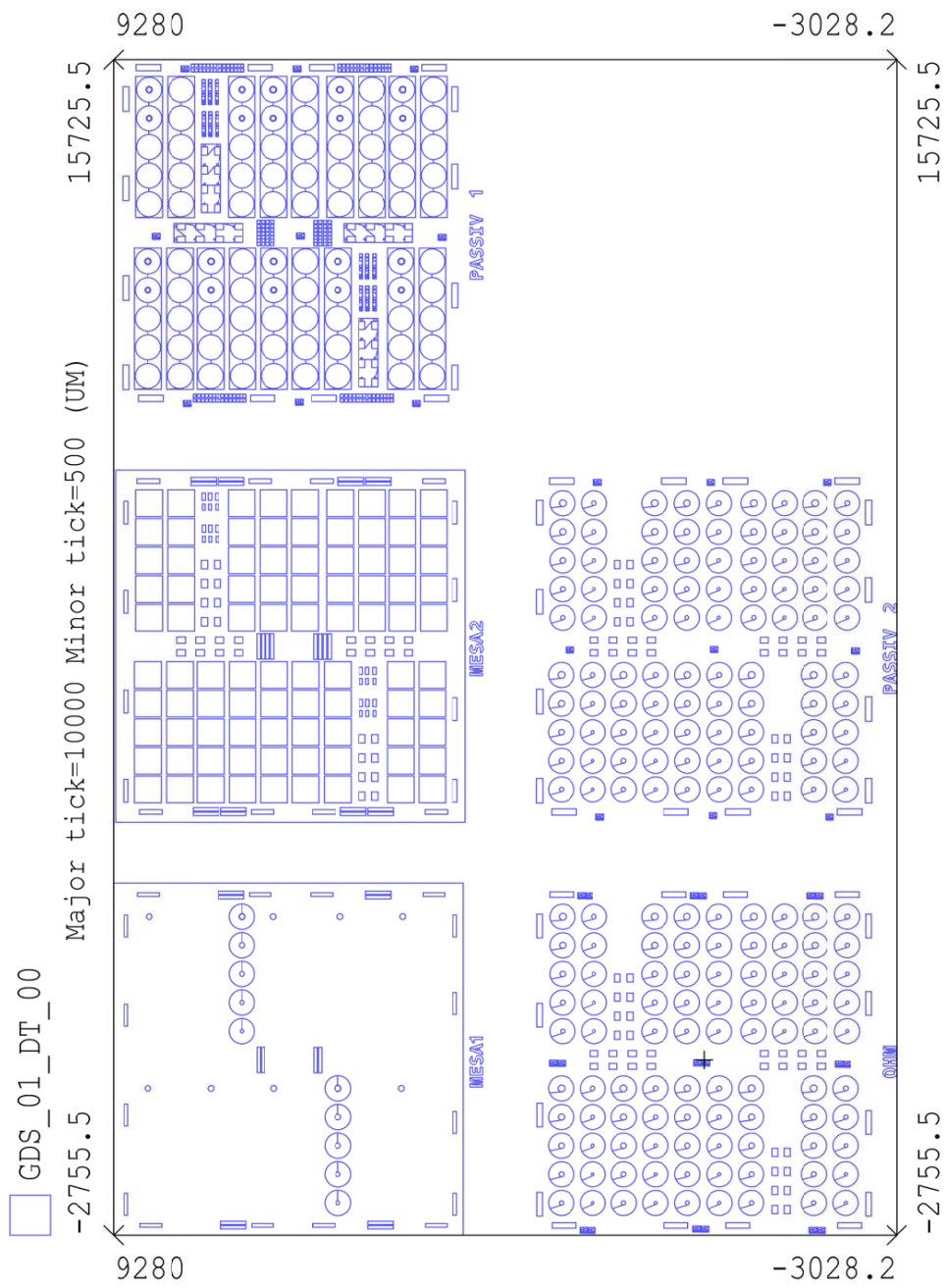
Figure B.4: HFE Diode Mask by C. Jin SEP 2008

Index